Original Article

Corresponding author:
Hannes Hofmann;
Email: hannes.hofmann@gfz-potsdam.de

CAMBRIDGE UNIVERSITY PRESS

Thermo-hydro-mechanical simulation of cooling-induced fault reactivation in Dutch geothermal reservoirs

Bakul Mathur[1], Hannes Hofmann[2,3] , Mauro Cacace[2], Gergő András Hutka[2] and Arno Zang[2,4]

[1]Friedrich-Alexander-Universität Erlangen-Nürnberg, Erlangen, Germany; [2]Helmholtz Centre Potsdam GFZ - German Research Center for Geosciences, Potsdam, Germany; [3]Technische Universität Berlin, Berlin, Germany and [4]Universität Potsdam, Potsdam, Germany

Abstract

Geothermal energy is one of the most viable sources of renewable heat. However, the potential risk of induced seismicity associated with geothermal operations may slow down the growth of the geothermal sector. Previous research has led to significant progress in understanding fluid-injection-induced seismicity in geothermal reservoirs. However, an in-depth assessment of thermal effects on the seismic risk was generally considered to be of secondary importance. This study aims to investigate the relative influence of temperature and key geological and operational parameters on the slip tendency of pre-existing faults. This is done through coupled thermo-hydro-mechanical simulations of the injection and production processes in synthetic geothermal reservoir models of the most utilized and potentially exploitable Dutch geothermal reservoir formations: Slochteren sandstone, Delft sandstone and Dinantian limestone.

In our study, changes in the slip tendency of a fault can largely be attributed to thermo-elastic effects, which confirms the findings of recent studies linking thermal stresses to induced seismicity. While the direct pore pressure effect on slip tendency tends to dominate over the early phase of the operations, once pore pressure equilibrium is established in a doublet system, it is the additional stress change associated with the growing cold-water front around the injection well that has the greatest influence. Therefore, the most significant increase in the slip tendency was observed when this low-temperature front reached the fault zone. The distance between an injection well and a pre-existing fault thus plays a pivotal role in determining the mechanical stability of a fault. A careful selection of a suitable target formation together with an appropriate planning of the operational parameters is also crucial to mitigate the risk of induced seismicity. Besides the well-known relevance of the in situ stress field and local fault geometry, rock-mechanical properties and operation conditions exert a major influence on induced stress changes and therefore on the fault (re)activation potential during geothermal operations.

Introduction

The worldwide geothermal power capacity amounts to 15.4 gigawatts (GW) as of 31 December 2019 (Richter, 2019). In the Netherlands, 24 geothermal doublets have been realized as of 1 January 2019 (Mijnlieff, 2020). The geothermal reservoirs in the Netherlands are the same as the ones targeted for oil and gas. With a geothermal gradient of approximately 31°C/km and an average surface temperature of 10°C (Bonte et al., 2012), the subsurface between 1.5 and 3.0 km depth is considered suitable for geothermal exploitation with temperatures ranging between 60 and 100°C. The majority of the installed doublets in the Netherlands target porous and permeable sandstone reservoirs including the Rotliegend, the Lower Germanic Triassic and the Upper Jurassic/Lower Cretaceous primarily in the West Netherlands Basin (Bekesi et al., 2020).

In this study, the Slochteren formation (part of the Permian deposits of the Upper Rotliegend group) was selected as the primary sedimentary geothermal reservoir of interest, because it is widely used for geothermal energy production and it extends throughout the Netherlands. Additionally, the Delft sandstone member (Lower Cretaceous), as a local porous sedimentary reservoir, and the Dinantian limestone (Carboniferous), as deep fracture/karst dominated geothermal reservoir, were investigated in this study. The latter formation could potentially serve as a target for a future enhanced geothermal system (EGS). Currently, no such projects are in operation in the Netherlands. However, the large potential of these systems, ongoing research (e.g. Moore et al., 2019; Huenges et al., 2020) and recent breakthroughs in EGS technology (Norbeck et al., 2023) could lead to a future use of the Dinantian limestone.

No major induced seismic events have yet been recorded in any of the Dutch geothermal sites in hot sedimentary aquifers Buijze (2020). The only reported seismicity related to geothermal operations in the Netherlands are events with a maximum magnitude of 1.7 at the Californië site,

which accesses a deep fault zone in the Dinantian limestones (Vörös & Baisch, 2022). Nevertheless, the possibility of induced seismicity inhibits an even faster development of the geothermal sector. Induced seismicity refers to seismic events caused by human interventions (Foulger et al., 2018). These seismic events are a direct result of changes of the stress state in the subsurface causing rapid slip along a pre-existing region of weakness (faults/ fractures). If the in situ stresses are close to a critical state with respect to the orientation of major faults, even a relatively small change in stresses may lead to seismic (or aseismic) failure of a fault.

In this study, coupled thermo-hydro-mechanical (THM) simulations were carried out to analyse the impact of various geological and operational parameters on the failure potential of a pre-existing fault in typical Dutch geothermal reservoirs. The THM computations were performed with the multi-physics, multi-component open source simulator GOLEM (Jacquey & Cacace, 2017; Cacace & Jacquey, 2017). The relative influence of key geological and operational parameters on the slip tendency of pre-existing faults was investigated with a sensitivity analysis in a synthetic geothermal reservoir model of the Slochteren sandstone formation, the Delft sandstone formation and the Dinantian limestone formation in the Netherlands. Among those parameters, a focus of our study is on the effect of re-injection temperature and related stress changes on fault stability, which likely plays a major, yet often ignored, role in injection-induced seismicity (Ghassemi et al., 2007; De Simone et al., 2013; Wassing et al., 2021; Kivi et al., 2022).

Numerical approach

The simulation code GOLEM uses a Galerkin Finite Element technique to solve for the parallel implicit non-linear coupled initial-boundary value problem. Balance equations of fluid and solid mass, heat and momentum serve as the base for the numerical formulations of the governing equations for fluid-flow, heat transport and elastic deformation (Cacace and & Jacquey, 2017).

Darcy's law correlates the Darcy's flow rate per unit of surface area or Darcy velocity (q_D) with porosity (n), fluid velocity (v_f) and solid velocity (v_s) and by expansion with the reservoir permeability (k), fluid viscosity (μ_f), pore-fluid pressure (p_f), fluid density (ρ_f) and acceleration due to gravity (g).

$$q_D = n(v_f - v_s) = -\frac{k}{\mu_f} . (\nabla p_f - \rho_f g) \qquad (1)$$

The mechanical governing equation is given by

$$\nabla . (\sigma' - \alpha p_f I) + \rho_b g = 0 \qquad (2)$$

where σ' denotes the effective stress, α denotes the Biot's coefficient of the reservoir rock, ρ_b denotes the bulk density of the rock-fluid system and I is an identity matrix. The effective stress is given by Equation (3).

$$\sigma' = \sigma + \alpha p_f I \qquad (3)$$

The change in the effective thermal stress for non-isothermal deformation is proportional to the drained thermal expansion coefficient (β_d), the material stiffness matrix (C) and the change in temperature (ΔT).

$$\Delta \sigma'_T = \frac{1}{3} C \beta_d \Delta T I \qquad (4)$$

The equation of internal energy conservation consists of the temporal, convective and conductive parts.

$$(\rho c)_b \frac{\partial T}{\partial t} + (\rho c)_f q_D \nabla T - \nabla . (\lambda_b \nabla T) = 0 \qquad (5)$$

where $(\rho c)_b$ denotes the bulk specific heat, $(\rho c)_f$ is the fluid specific heat and λ_b denotes bulk thermal conductivity.

The problem variables are pore fluid pressure, temperature and solid displacement, which results in a system of non-linear coupled equations. A detailed derivation of the formulations is described in Cacace & Jacquey (2017). A weighted residual method is then applied to the system of equations to obtain the weak forms of these governing equations. The weak forms of the governing equations are solved either by Newton–Raphson or Free Jacobian Inexact Newton Krylow schemes (Cacace & Jacquey, 2017).

The fault failure potential is estimated in terms of a parameter referred to as 'slip tendency' (ST), which is defined as the ratio of the resolved shear stress (τ) and the effective normal stress ($\sigma'_n = \sigma_n - p_f$) on the fault plane (Morris et al., 1996; Ramsay & Lisle, 2000).

$$ST = \frac{\tau}{\sigma'_n} \qquad (6)$$

The Mohr–Coulomb criterion is used to determine the failure of a fault plane. It states that slip occurs when the shear stress along the fault plane exceeds the static shear strength of the fault, which is given in terms of the fault friction coefficient (μ_s) and cohesion (S_o) as follows:

$$\tau \geq S_o + \mu_s . \sigma'_n \qquad (7)$$

For a cohesionless fault ($S_0 = 0$) slip occurs when

$$ST \geq \mu_s \qquad (8)$$

In this study, the static friction coefficient of the fault was taken as 0.6. A slip tendency value higher than 0.6 was therefore considered as an indication of fault failure.

We note that the slip tendency only gives a probability of (re) activation of the fault without providing information on whether the resulting fault is seismic or aseismic. Therefore, we performed an additional study, considering a rate and state formalism to describe the frictional behaviour of the fault, which we discuss in the supplementary text (Figures S1–S4). In addition, we refer to a companion study by Hutka et al. (2023) that uses the same model geometry and a different method introduced by Cacace et al. (2021) to quantify the seismic response of the reservoir in the same scenarios presented in this study.

Model setups and scenarios

The THM simulation including slip tendency analysis with GOLEM has been validated at the Groß Schönebeck (GrSk) EGS site (Blöcher et al., 2018). This site accesses the Rotliegend formation below ~3900 m.

The validated model was adapted to the condition in the different formations of interest in the Netherlands. All reservoir
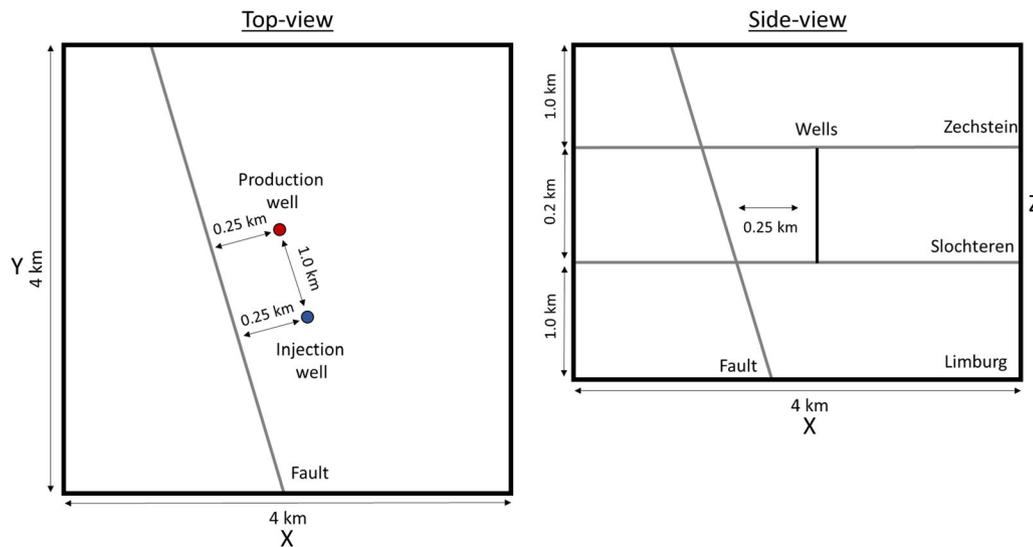
Figure 1. Top view (top left) and side view (top right) for the Slochteren base case model (not to scale).

models were setup in a similar fashion. The coordinates of the model were aligned with the maximum (S_{HMax}) and minimum horizontal stress directions (S_{hmin}). This was done to avoid any shear stress accumulation along the edges of the model and the resulting distortion of the original model geometry. The finite element mesh was generated with the open source software MeshIt (Cacace & Blöcher, 2015). Mesh refinement was applied around the wellbores, along the fault and inside the reservoir unit. We used an adaptive time stepping, where the time step size increases with the number of nonlinear iterations at each time step with an upper bound of 1 year. A steady-state simulation run first to initialize the model in terms of pore pressure, temperature and relative displacements, consistent with the in situ reservoir conditions. This steady-state model was then used as starting model (initial conditions) for the subsequent transient runs covering a 30-year simulation period with cold water injection and production with the same flow rate.

Slochteren sandstone reservoir

The Slochteren sandstone model was simplified to three horizontal geological units: Zechstein (top seal unit), Slochteren (reservoir unit) and Limburg (bottom seal unit). All three units are intersected by a two-dimensional fault. The two wells are represented by one-dimensional line elements representing the open hole sections of the injection and production well, which intersect the entire reservoir unit. Figure 1 illustrates the top and side views of the Slochteren base case model. Figure 2 is a snapshot of the base case model mesh. Mechanical, hydraulic and thermal properties of the rock matrix of reservoir, top and bottom unit as well as fault properties can be found in Table 1. Fluid properties are summarized in Table 2. A summary of the model geometry and wellbore information is provided in Table 3. Detailed information on the boundary conditions are presented in Table 4.

Model geometry and boundary conditions

The top of the Slochteren reservoir varies between 1500 and 3000 m and its thickness varies between 100 and 250 m (Mijnlieff, 2020). We chose the Middenmeer site with a top Slochteren depth of 2200 m and a thickness of 200 m as representative for the base case model (DESTRESS, 2021). The thickness of the overlying

Zechstein group varies between <100 m (in marginal settings) and >1200 m (in the salt basin; TNO-GSN, 2021; Duin et al., 2006). The underlying Limburg group has typically a thickness of ~600 m which can reach up to 1300 m (Dinoloket, 2021). To avoid any boundary effects, we used a 1000 m thickness for both top and bottom layer.

Fault patterns are relatively homogeneous across the whole onshore part of the Netherlands with a main fault trend varying between NW-SE and NNW-SSE and faults dipping in different directions (Duin et al., 2006; de Jager, 2007). We do not consider secondary fault systems that strike in different directions and we consider only a dip towards NE. Cross-sections in de Jager (2007) show that most faults are sub-vertical. Thus, we assume a typical fault dip of 80° and tested variations in the dip angle between 60° and 85°.

The average temperature gradient in the Netherlands can be considered as 31°C/km with a surface temperature of 10°C and an uncertainty of ±10°C/km (Bonté et al., 2012). We therefore use 31°C/km + 10°C for the base case, 20°C/km + 10°C as minimum and 40°C/km + 10°C as maximum temperature gradient. Despite the possibility of local fluid overpressures (Verweij et al., 2012), we assume an initial hydrostatic pore pressure gradient in our simulations. For this, we assume a minimum density of 1020 kg/m³, representative for seawater, and a maximum density of 1220 kg/m³, representative for a brine with salinity of ~400 g/l, which is rarely exceeded in the Dutch Rotliegend (Veldkamp et al., 2016). This corresponds to minimum and maximum pore pressure gradients of 10 and 12 MPa/km. For the base case scenario, we chose 11 MPa/km, representative for the GrSk geothermal site with 265 g/l salinity (Blöcher et al., 2010).

We assume a normal faulting regime (SV > SHmax > Shmin) according to Guises et al. (2015). According to Verweij et al. (2012), the vertical stress gradient in the Netherlands is frequently below the standard gradient of ~23 MPa/km (corresponding to ~2300 kg/m³ bulk density). Van Eijs (2015) shows vertical stress gradients increase with depth from ~19 to 21 MPa/km at 1 km depth to 22–24 MPa/km (at 3 km depth). We therefore assume an average vertical stress gradient of 22 MPa/km for the base case scenario with a possible variation between 21 and 23 MPa/km. Note that these are average gradients over the entire depth range and only the corresponding effective horizontal stress values at a point located

Table 1. Mechanical, thermal and hydraulic properties of geological units and the fault in the Slochteren sandstone base case model.

Model property	Zechstein (rock salt)	Rotliegend (sandstone)	Limburg (claystone)	Fault
Young's modulus (GPa)	30	15	40	15
Poisson's ratio (-)	0.3	0.2	0.2	0.2
Solid bulk modulus (GPa)	30	40	50	40
Drained bulk modulus (GPa)	25	8.33	22.2	8.33
Biot coefficient (-)	0.17	0.86	0.56	0.86
Friction coefficient (-)	–	–	–	0.6
Cohesion (MPa)	–	–	–	0
Solid thermal conductivity (W/m/°C)	4.5	3.5	2.0	3.5
Solid heat capacity (J/kg/°C)	925	830	860	830
Volumetric bulk thermal expansion coefficient (1e-6/°C)	30	30	30	30
Solid density (kg/m³)	2170	2650	2650	2650
Hor. permeability (mD)	0.001	100	0.001	100
Hor./vert. permeability (-)	1	2	1	1
Porosity (%)	1	20	1	100
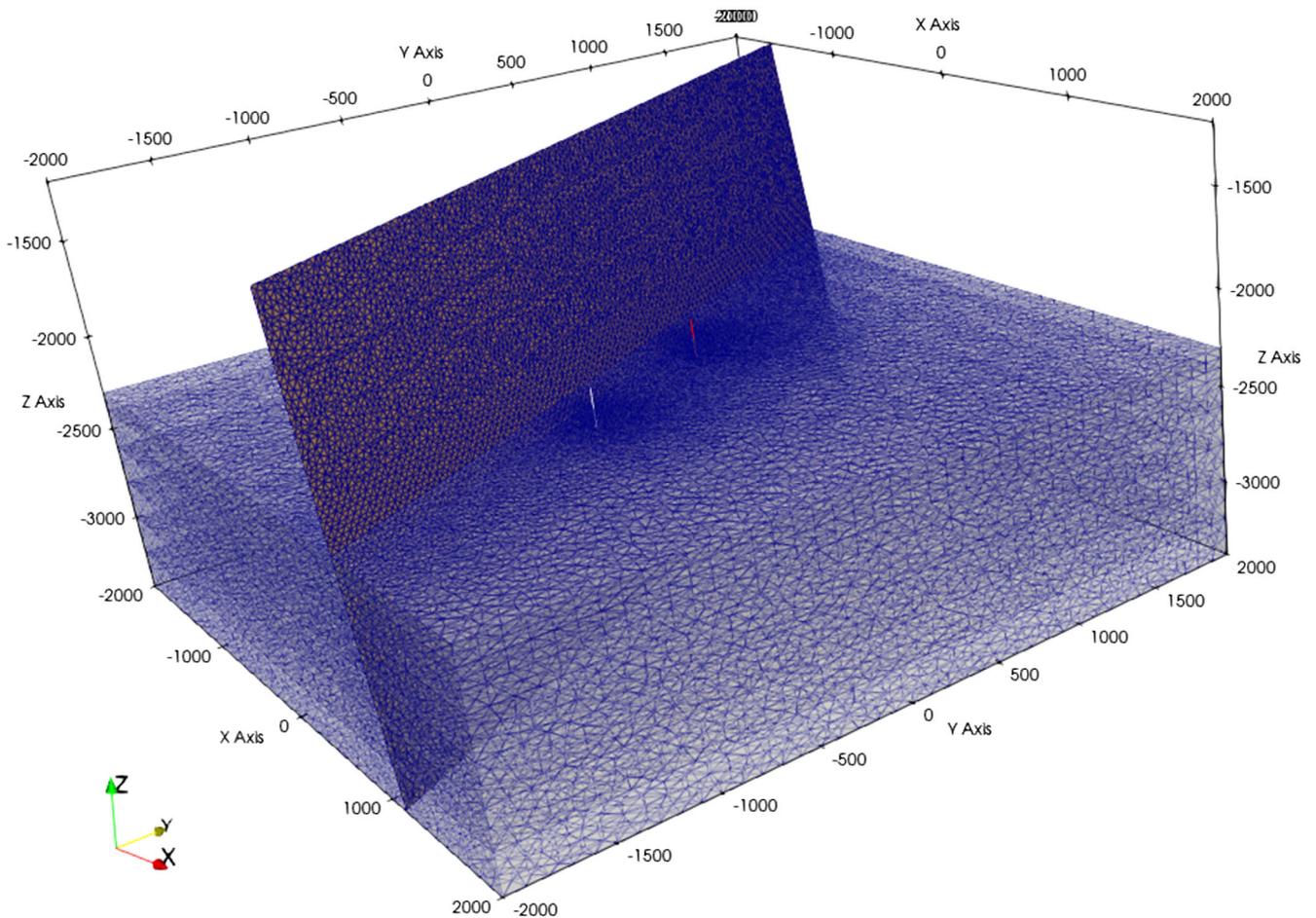
Figure 2. 3D view of the Slochteren base case mesh. Mesh refinement is applied around the injection and production wells and in the fault plane within the reservoir unit.

Table 2. Fluid properties of the Slocheren sandstone, Delft sandstone and Dinantian limestone models. The viscosity for the Slochteren and Dinantian models is a function of pressure and temperature derived from the data from the Groß Schönebeck Rotliegend reservoir fluid. In the Delft models, a pressure and temperature dependent viscosity function for pure water was used.

Fluid property	Slochteren sandstone model	Delft sandstone model	Dinantian limestone model
Density (kg/m³)	1154	1154	1154
Viscosity (mPas)	$f(P/T)_{GrSk}$	$f(P/T)_{H2O}$	$f(P/T)_{GrSk}$
Specific heat capacity (J/kg/°C)	3240	4125	3240
Thermal conductivity (W/m/°C)	0.625	0.65	0.625
Bulk modulus (GPa)	3.4	2.35	3.4

Table 3. Geometrical and wellbore properties of the Slochteren sandstone model (base case scenario).

Model property	Zechstein (rock salt)	Rotliegend (sandstone)	Limburg (claystone)
Unit top (m)	2000	2200	2400
Unit thickness (m)	1000	200	1000
Fault strike		N130°E	
Fault dip (° from horizontal)		80	
Fault dip direction		NE	
Well length (m)	–	200	–
Well diameter (m)	–	0.05	–
Well permeability (m²)	–	3.12e-4	–
Well porosity (-)	–	1	–

at the centre of the Slochteren formation are used for model calibration. The actual stress gradients in the individual layers depend on the elastic rock properties.

According to TNO (2015), the standard minimum horizontal stress gradient can be considered as 0.6 times the standard vertical gradient of 23 MPa/km (ΔShmin = 13.8 MPa/km). They find that the leak-off pressure, which is representative for the minimum horizontal stress, is rarely below this standard gradient and is also bound by the lithostatic stress gradient. Osinga & Buik (2019) propose a Shmin gradient of 18 MPa/km for the deeper Dinantian formation. Guises et al. (2015) determined minimum horizontal stress gradients of 15.4–16.7 MPa/km for the Groningen gas field. We assume a minimum horizontal stress gradient of 14 MPa/km for the base case scenario with 13 MPa/km and 20 MPa/km as lower and upper bound, respectively.

Van Eijs (2015) found relatively low differences between the minimum and maximum horizontal stress gradients in the Groningen gas field. Different methods yield a variation of the ratio SHmax/Shmin between 1.02 and 1.42. Osinga & Buik (2019) suggested SHmax as ~5–20% higher than Shmin as a reference. Guises et al. (2015) determined maximum horizontal stress gradients of 17.3–18.2 MPa/km for the Groningen gas field. We assume a typical SHmax/Shmin ratio of 1.07 for the base case scenario (ΔSHmax = 1.07 * 14 MPa/km = 15 MPa/km), a lower bound for the SHmax gradient equal to the minimum horizontal stress gradient (14 MPa/km) and an upper bound of the SHmax gradient equal to 20 MPa (ΔSHmax = 1.42 * 14 MPa/km = 20 MPa/km). Note that SHmax has the largest uncertainty among all stress magnitudes.

According to Mechelse (2017), the pre- and post-salt stress directions are similar. The maximum horizontal stress direction in the Netherlands is typically NW-SE with values ranging between N130°E and N5°E (Heidbach et al. 2016). Guises et al. (2015) determined the maximum horizontal stress direction to be N160°E in the Groningen gas field. We assume N160°E for the base case scenario and a typical range between N150°E and N170°E for the sensitivity analysis. Note that stress directions may strongly vary locally since stress rotations can be expected near salt domes

Table 4. Slochteren sandstone, Delft sandstone and Dinantian limestone base case model boundary conditions.

Parameter	Value	Boundary condition
Temperature gradient	31°C/km + 10°C	Constant temperature at top and bottom boundary
Pore-pressure gradient	11 MPa/km	Constant pressure gradient on all four vertical boundaries
Vertical stress gradient	23 MPa/km	Constant stress in z-direction on top boundary and no displacement in z-direction on bottom boundary
Maximum horizontal stress gradient	15 MPa/km	Constant displacement in y-direction on front boundary and no displacement in y-direction on back boundary
Minimum horizontal stress gradient	14 MPa/km	Constant displacement in x-direction on left boundary and no displacement in x-direction on right boundary
Maximum horizontal stress direction	N160°E	Model boundaries aligned with maximum horizontal stress direction by rotation
Injection rate	70 L/s	Constant injection rate applied to the middle point of the injection well (only during dynamic simulation, not applied to steady state)
Produciton rate	70 L/s	Constant production rate applied to the middle point of the production well (only during dynamic simulation, not applied to steady state)
Injection temperature	30°C	Constant temperature applied to the middle point of the injection well (only during dynamic simulation, not applied to steady state)

and fault zones, which we do not consider in our sensitivity analysis.

According to Mijnlieff (2020), the flow rate of geothermal wells accessing the Slochteren reservoir ranges from ~40 to ~100 l/s. We chose these values as lower and upper limits, respectively, and their median value of 70 l/s as representative for the base case scenario.

The well spacing (distance between production and injection well) is typically calculated as to avoid thermal breakthrough during the projected lifetime of the doublet. The well spacing of Dutch geothermal doublets is up to 1.5 km (Mijnlieff, 2020). We therefore use 1.5 km as maximum well spacing. For the base case, we use a typical well spacing of 1 km and 0.5 km represents our lower bound for the sensitivity analysis.

Typically, a re-injection temperature of 25–35°C can be assumed for Dutch geothermal wells (Hurter & Schellschmidt, 2003; Wang et al., 2019; Willems et al., 2017). We use a re-injection temperature of 30°C for the base case scenario. To evaluate the effect of the re-injection temperature, we use 20°C and 70°C as lower and upper bound.

We do not model the entire geothermal wellbores explicitly but approximate them as open 1D elements going through the entire reservoir layer. Therefore, we do not consider the wellbore diameter in our sensitivity analysis. However, we use a typical geothermal wellbore diameter of 8 ½" for the open hole section in all models.

We use a relatively short distance between wells and fault of 250 m for the base case scenario in order to easily see effects of different parameters on the temperature, pressure and stress distribution on the fault. For the sensitivity analysis, we vary this distance between 0 m (well intersects the fault) and 1000 m.

Rock matrix, fault and fluid properties
Geomechanical rock properties
Solid bulk modulus. The Slochteren reservoir sandstone primarily consists of quartz. According to Schmitt (2015), the solid bulk modulus of Quartz is 37.8 GPa (α-Quartz) and 42.97 GPa (β-Quartz). We assume a solid bulk modulus of 40 GPa for the Rotliegend sandstone in the base case model. The Zechstein group may consist of calcite, dolomite, anhydrite and halite with a solid bulk modulus of 73.3 GPa, 94.9 GPa, 54.9 GPa and 24.9 GPa, respectively (Schmitt, 2015). We assume a solid bulk modulus of 30 GPa for the Zechstein formation in the base case model. Claystones, which we assume representative for the Carboniferous in our model, primarily consist of illite, smectite (Montmorillonite) and kaolinite. The solid bulk modulus of muscovite, dry Na montmorillonite, wet montmorillonite and kaolinite is 58.2 GPa, 82 GPa, 36 GPa and 71.1 GPa, respectively (Schmitt, 2015). We assumed a solid bulk modulus of 50 GPa, representative for clay according to Delage (2013) for the Carboniferous Limburg claystone formation.

Young's modulus and Poisson's ratio. Lele et al. (2015) performed a geomechanical modelling study of the Groningen gas field.

For the Rotliegend reservoir Lele et al. (2015), use a porosity-dependent Young's modulus and Poisson's ratio with values of 10 GPa and 0.18, respectively, at 20% porosity and a variation between 1 and 35 GPa and between 0.05 and 0.25, respectively. Zang et al. (1996) determined the Young's modulus of several Flechtingen sandstone samples and found values between 14 and 29 GPa for dry samples and between 12 and 24 GPa for wet samples. Pijnenburg et al. (2019) determined Young's moduli

between 3 and 22 GPa for Slochteren sandstone depending on the porosity and the effective confining pressure. They also find typical values for Poisson's ratio close to 0.2. We therefore assume base case values for the Slochteren sandstone unit of $E = 10$ GPa and $\nu = 0.2$ with upper and lower bounds between 3 and 30 GPa for Young's modulus and 0.1 and 0.25 for Poisson's ratio.

For the Zechstein Halite Lele et al. (2015) use a Young's modulus of 30 GPa and a Poisson's ratio of 0.35 while they use a Young's modulus of 40 GPa and a Poisson's ratio of 0.2 for the Carboniferous. We use the same parameters for the base case model in our study except for the Poisson's ratio of the Zechstein, where we used 0.3 for consistency with the Biot coefficient α.

Biot coefficient. Biot's coefficient α is not a direct parameter assigned to the model, but it is computed internally as a function of the drained bulk modulus $K = E/(3(1 − 2\nu))$ (with Young's modulus E and Poisson's ratio ν) and solid bulk modulus K_s (measured), as: $\alpha = 1 − K/K_s$. Using these formulas, we determined the drained bulk modulus and the Biot coefficient in Table 1 and checked all values for internal consistency and consistency with literature values.

For the Slochteren sandstone model this yields a Biot coefficient of 0.86 for the base case model and a range between 0.5 and 0.97. This is consistent with the values used by Lele et al. (2015).

Based on laboratory experiments, Zhang et al. (2018) found that rock salt may actually show a weak poromechanical behaviour corresponding to relatively low values of the Biot coefficient in the order of 0.2–0.3. Missal (2019) reported a Biot coefficient of intact rock salt of ~0.4 and that of damaged rock salt as ~1. However, Biot's coefficient of rock salt may be as low as 0.12 according to Kansy (2007). Using a solid bulk modulus of 30 GPa, a Young's modulus of 30 GPa and a Poisson's ratio of 0.3 yields a Biot coefficient of 0.17 for the Zechstein, consistent with a low-porosity rock salt formation.

The Biot coefficient of the Limburg group is difficult to assess. However, the Young's modulus of 40 GPa, Poisson's ratio of 0.2 and solid bulk modulus of 50 GPa yield a Biot coefficient of 0.56 for the Limbourg group (claystone). Both elastic properties of the Zechstein and Limburg groups may vary significantly depending on the local mineralogical composition.

Hydraulic rock properties
Porosity and permeability. The (horizontal) permeability of the exploited Rotliegend reservoirs is between 50 and 350 mD according to Mijnlieff (2020). Given that a minimum tranmissivity (permeability*thickness) of 10–15 Dm is required for a successful project (Mijnlieff, 2020) and considering a typical thickness of 200 m, we assume 100 mD as a representative base case scenario, corresponding to 20 Dm transmissivity. However, the vertical permeability is typically 2–10 times lower compared to the horizontal permeability (e.g. Doddema, 2012; Mohammed, 2020). We use a ratio between horizontal and vertical permeability of 2 for the base case scenario and a range between 1 and 10 in the sensitivity analysis. According to Lele et al. (2015) and Pijnenburg et al. (2019), Rotliegend sandstone porosity may range approximately between 10 and 30%. We use 20% for the base case scenario. Both Zechstein rock salt and Limburg claystone can be considered as nearly impermeable formations. Therefore, we assume a horizontal and vertical permeability of 0.001 mD and a porosity of 1% for both formations.

Thermophysical rock properties

Thermal conductivity. For the Rotliegend reservoir, Daniilidis et al. (2016) use a wet thermal conductivity of 2.9 W/m/K. Doddema (2012) found values for sandstone mostly between ~2.5 and ~3.5 W/m/K and used 3.0 W/m/K as wet heat conductivity of the Rotliegend reservoir layer. Considering a porosity of 20% and a thermal conductivity of 0.63 W/m/K (water at 20°C), one arrives at solid heat conductivities between ~3 and 4.2 W/m/K. Blackwell & Steele (1989) provide thermal conductivity values of sandstones between 2.5 and 4.2 W/m/K. Fuchs et al. (2015) report thermal conductivity values of 7.7 W/m/K for quartz, 2–2.33 W/m/K for micas and 1.9–2.25 W/m/K for feldspars. We assume a solid heat conductivity of the Slochteren sandstone reservoir of 3.5 W/m/K with a possible range between 3.0 and 7.7 W/m/K.

The thermal conductivity of halite crystals is ~5.5 W/m/K at 50°C. It varies between ~4.5 W/m/K at 100°C and ~6 W/m/K at 25°C (Urquhart & Bauer, 2015). Fuchs et al. (2015) even report 6.5 W/m/K for halite. Daniilidis et al. (2016) use a wet heat conductivity of 3.5 W/m/K for the Zechstein salt in their model, while Doddema (2012) use a value of 5.5 W/m/K. We assume a solid thermal conductivity of 4.5 W/m/K for the Zechstein salt layer.

The Limburg layer is assumed to consist preferentially of claystone in our model. Clays have thermal conductivities between 1.8 and 1.85 W/m/K (montmorillonite and Illite) and 2.7 W/m/K (kaolinite) according to Fuchs et al. (2015). Daniilidis et al. (2016) use a wet heat conductivity of 2.65 W/m/K and Doddema (2012) uses 2.0 W/m/K for the Limburg group. While claystone thermal conductivities are ~2 W/m/K in the literature study of Doddema (2012), they also find higher values of 2.5–4 W/m/K for the Carboniferous. We assume a thermal conductivity of 2.0 W/m/K for the Limburg group.

Solid heat capacity. The heat capacity of quartz generally increases with temperature. Waples & Waples (2004) report a solid heat capacity of quartz of 740 J/kg/K at 20°C. Feldspars have heat capacities of 630–800 J/kg/K at 20°C (Waples & Waples, 2004) and plagioclase has a heat capacity between 711 and 837 J/kg/K at 20°C (Waples & Waples, 2004). For Quartzite and Microquartzite Waples & Waples (2004) report values of 1013 J/kg/K and 950 J/kg/K at 20°C. Daniilidis et al. (2016) use a heat capacity of 827 J/kg/K for their Rotliegend reservoir model and Doddema (2012) use 870 J/kg/K with a range of values determined from literature sources mainly between ~700 and ~1050 J/kg/K for sandstones. Given that our reservoir has an elevated temperature, we assume a base case solid heat capacity of the Slochteren sandstone reservoir of 830 J/kg/°C with possible values between 650 and 1050 J/kg/°C.

The solid heat capacity of halite crystals lies between 1920 J/m³/K (885 J/kg/K) and 2050 J/m³/K (945 J/kg/K) with no temperature dependence (Urquhart Bauer, 2015). Waples & Waples (2004) report a solid heat capacity of 926 J/kg/K at 25°C. Daniilidis et al. (2016) and Doddema (2012) adopt a heat capacity of 1050 J/kg/K in their model of the Zechstein salt layer (combined heat capacity of solid and fluid). We use a solid heat capacity of 925 J/kg/K for the Zechstein layer.

The heat capacity of clay is 860 J/kg/K at 20°C according to Waples & Waples (2004). Daniilidis et al. (2016) use a heat capacity of 840 J/kg/K for the Limburg formation and Doddema (2012) used a value of 870 J/kg/K for the Carboniferous. We therefore assume a solid heat capacity of 860 J/kg/K for the Limburg formation.

Thermal expansion coefficient. The volumetric solid thermal expansion coefficient is approximately three times the linear solid thermal expansion coefficient for isotropic rocks and minerals. The undrained bulk thermal expansion coefficient can be expressed as $\alpha_{bu} = \alpha_s + \Phi B(\alpha_f - \alpha_s)$, with porosity Φ, Skempton coefficient B, solid (mineral) volumetric thermal expansion coefficient α_s and the volumetric thermal expansion coefficient of the fluid α_f (McTigue, 1986). This would be representative of heating or cooling of rock with isolated (non-connected) pore space. In our model, this is representative for the top seal (Zechstein) and the basement (Limburg). Since the porosity of these formations is negligible (1%), the effective bulk thermal expansion coefficient of the rock can be considered approximately equal to the solid volumetric thermal expansion coefficient.

The drained bulk thermal expansion coefficient of a fluid-saturated rock is equal to the bulk thermal expansion coefficient of dry rock (Jaeger et al., 2007). The drained bulk thermal expansion coefficient is representative for a porous and permeable geothermal sandstone reservoir, in our case the Slochteren sandstone reservoir. The drained volumetric bulk thermal expansion coefficient can be determined in the laboratory. The solid grain volumetric thermal expansion coefficients are also known.

The effect of the thermal expansion on the pore pressure is governed by the difference between the thermal expansion coefficients of pore fluid α_f and pore volume α_p (Zimmerman, 2000). This coupling is neglected in our simulations.

The volumetric thermal expansion coefficient of quartz is equal to 33.4e-6 1/°C (Palciauskas & Domenico, 1982). At higher temperatures, this value slightly increases (37.2e-6 1/°C at 80°C based on Falzone & Stacey, 1982). The average thermal expansion coefficient of feldspars is 11.1e-6 1/°C (Fei, 1995), the solid thermal expansion coefficient of clay is 34e-6 1/°C (McTigue, 1986) and the solid thermal expansion coefficient of salt is between 120e-6 1/°C (McTigue, 1986) and 140e-6 1/°C (Skinner, 1966). For calcite, similar values are reported as for quartz (Srinivasan, 1955). Somerton (1992) report a linear thermal expansion coefficient of quartz of 16 e-6 1/°C and linear thermal expansion coefficients of Berea, Bandera and Boise sandstone of 15e-6 to 16e-6 1/°C under dry conditions and 13e-6 to 20e-6 1/°C under saturated conditions. The drained bulk volumetric thermal expansion coefficient of Rothbach sandstone was measured as 28e-6 1/°C and calculated as 29.7e-6 1/°C by Ghabezloo & Sulem (2009). Hassanzadegan et al. (2012) determined a solid volumetric thermal expansion coefficient of a 10% porosity Flechtinger Sandstone to be 27.2e-6 1/°C. Plevová et al. (2011) determined thermal expansion coefficients of different Czech sandstones to be ~20e-6 1/°C. Zoback (2007) reports linear thermal expansion data from Griffith (1936). These values include ~10e-6 1/°C (α_v ~ 30e-6 1/°C) for Sandstones, ~11e-6 1/°C (α_v ~ 33e-6 1/°C) for quartzites and cherts, ~6.5e-6 1/°C (α_v ~ 19.5e-6 1/°C) for andesites and ~8e-6 1/°C (α_v ~ 24e-6 1/°C) for slates. Zoback (2007) states that the linear thermal expansion coefficient of silica is ~10e-6 1/°C (α_v ~ 30e-6 1/°C) while it is ~1e-6 1/°C (α_v ~ 3e-6 1/°C) for most other rock forming minerals. Slizowski et al. (2015) determined volumetric thermal expansion coefficients of 43e-6 to 54e-6 1/°C for polish Zechstein salt aggregates in laboratory experiments for the temperature range 20–100°C. The volumetric thermal expansion coefficient of anhydrite at room temperature was determined as 36.6e-6 1/°C by Evans (1979). Zhang et al. (2007) use a thermal expansion coefficient of Monfared et al. (2011) who determine the solid thermal expansion coefficient of Opalinus claystone as 30e-6 1/°C.

Zhang et al. (2007) modelled experiments on Opalinus clay with bulk ('wet') linear thermal expansion coefficients of 15e-6 1/°C by using a fluid volumetric thermal expansion coefficient of 340e-6 1/°C and a solid linear thermal expansion coefficient of 1.5e-6 1/°C.

As indicated above, for the low porosity Zechstein and Limburg formations, we assume that the bulk volumetric thermal expansion coefficient equals to the solid volumetric thermal expansion coefficient of the minerals as suggested by Palciauskas & Domenico (1982). The thermal expansion coefficients of liquid-saturated sandstones are not much different from dry sandstones (Somerton, 1992). Also, no large differences were found between the thermal expansion coefficients of quartz and sandstones. Therefore, we also assume that bulk thermal expansion coefficient is equal to solid thermal expansion coefficient for the Slochteren sandstone formation.

For the base case scenario, we use a bulk volumetric thermal expansion coefficient of 30e-6 1/°C for all three layers with a potential variability in the Slochteren sandstone between 20e-6 and 40e-6 1/°C. Even though Halite has a volumetric thermal expansion coefficient of 120e-6 1/°C, the Zechstein is a very complex formation including additionally anhydrite ($\alpha_v \sim$ 37e-6 1/°C), carbonates ($\alpha_v \sim$ 12-36e-6 1/°C) and claystones ($\alpha_v \sim$ 30e-6 1/°C). Additionally, a much lower volumetric thermal expansion coefficient was determined for Zechstein rock samples in laboratory experiments ($\alpha_v \sim$ 43-54e-6 1/°C) and most other rock forming minerals have much lower thermal expansion coefficients in the order of 3e-6 1/°C. Since the solid thermal expansion coefficient of clay is similar to that of quartz, we also use 30e-6 1/°C for the Limburg formation.

Solid density. Quartz has a solid density of 2650 kg/m³ (Blake, 2008). This value is used for the Rotliegend reservoir layer in the base case model. Daniilidis et al. (2016) consider a density range of 2500–2700 kg/m³. We therefore adopt this range as approximate lower and upper bounds.

The solid density of halite is 2170 kg/m³. Daniilidis et al. (2016) use the same value for the Zechstein formation in their model. We therefore use a solid density of 2170 kg/m³ for the Zechstein layer. The actual solid density of the Zechstein layer may vary significantly (Doddema, 2012).

The density of clay minerals typically ranges between 2000 and 3000 kg/m³ while many are near 2650 kg/m³ (Blake, 2008). We therefore use 2650 kg/m³ as solid density of the Limburg layer.

Fault properties. The fault is modelled as planar discontinuity with finite aperture. Fault asperities and roughness are not considered. In the base case scenario, we assume that the fault has the same properties as the reservoir rock (100 mD permeability and 20% porosity). The fault aperture a is calculated from the permeability k using the cubic law: $a = \sqrt{12k}$. As upper and lower bound, we assume 0 and 100% porosity and 0 and 10 D permeability.

Hunfeld et al. (2017) determined fault friction coefficients of 0.66 for the Basal Zechstein, 0.37 for the Ten Boer claystone, 0.6 for the Rotliegend sandstone and 0.5 for the Carboniferous. Even though other researchers (Buijze et al., 2017) use different fault friction coefficients for the different units as determined from these laboratory experiments (Hunfeld et al., 2017, 2020) and some fault cohesion between 0 and 3 MPa, we assume a cohesionless fault with a uniform fault friction coefficient of 0.6 that lies approximately between 0.5 and 0.7 due to the inherent uncertainty in these parameters.

Reservoir fluid properties. The reservoir fluid is saline water (brine) with pressure- and temperature-dependent fluid properties. For the base case model, we use fluid density, viscosity, heat capacity and bulk modulus determined for the Groß Schönebeck (GrSk) site (NaCl, KCl and CaCl2 molality of 1.815, 0.043 and 1.399, respectively) using the code BrineProp_0.7.3.1 (Francke et al., 2013). A 5 mol NaCl/kg H2O solution, which has a similar salinity as the Groß Schönebeck fluid, was assumed for the volumetric thermal expansion coefficient and the thermal conductivity. Viscosity and thermal expansion coefficient have the largest temperature/pressure dependence. Additionally, considering the salinity is important for all other fluid properties. For the viscosity, a temperature and pressure dependent look-up table is used. Bulk modulus, density, thermal conductivity and heat capacity are almost not affected by pressure and temperature changes. Thus, constant values are assumed here. We do not explicitly implement fluid thermal expansion coefficients in the model, as these values are integrated into the pore thermal expansion coefficient.

For the sensitivity analysis we use the pressure and temperature dependent water properties from REFPROP (Lemmon et al., 2018) and typical variations within the expected salinity range of 0–400 g/l and pressure and temperature range.

Delft sandstone reservoir models

This section describes the hydrothermal reservoir properties above the Permian salt in the Netherlands. The considered reservoir formation is the Delft Sandstone Member. This massive sandstone sequence is overlain by the Rodenrijs Member, an organic rich claystone, which is used as the top layer in this model. The Alblasserdam Member (flood-plain deposits) is used as the bottom layer in this model.

Model geometry and boundary conditions

We simplify the geology to a conceptual model consisting of a horizontal claystone layer (Rodenrijs member) as top seal, a horizontal sandstone layer (Delft sandstone) as reservoir unit and a horizontal claystone layer (Alblasserdam member) lower bound. Again, all layers are intersected by a single inclined fault, and no fault offset is assumed. We note that, in contrast to our model, faults in nature usually share some degree of offset. Data from the Groningen gas field show that most mapped faults have an offset of up to 100 m, occasionally even more than 200 m (Buijze, 2020). However, with offset faults, there are discontinuities in the material properties on both sides of the fault, leading to peaks in shear and normal stresses at the intersections between formation and fault (e.g. Van Wees et al., 2017). Numerical simulations amplify these stress peaks due to simplified geometry (e.g. sharp material boundaries, no damage zone, planar fault) and mechanics (homogeneous linear elastic medium). In addition, the mesh size can influence the amplitude of the observed peaks (Jansen & Meulenbroek, 2022).

We therefore assumed zero-offset faults in our study to avoid these simplifications leading to numerical artefacts in the calculation of the slip tendency. This simplification allows us to analyse the relative impact of certain geological and operational scenarios on the (re)activation potential of faults. However, when interpreting the absolute values of the calculated slip tendencies, it is important to consider these limitations of our model.

Hot water production and cold-water injection are also modelled through a typical Dutch geothermal well doublet. Both
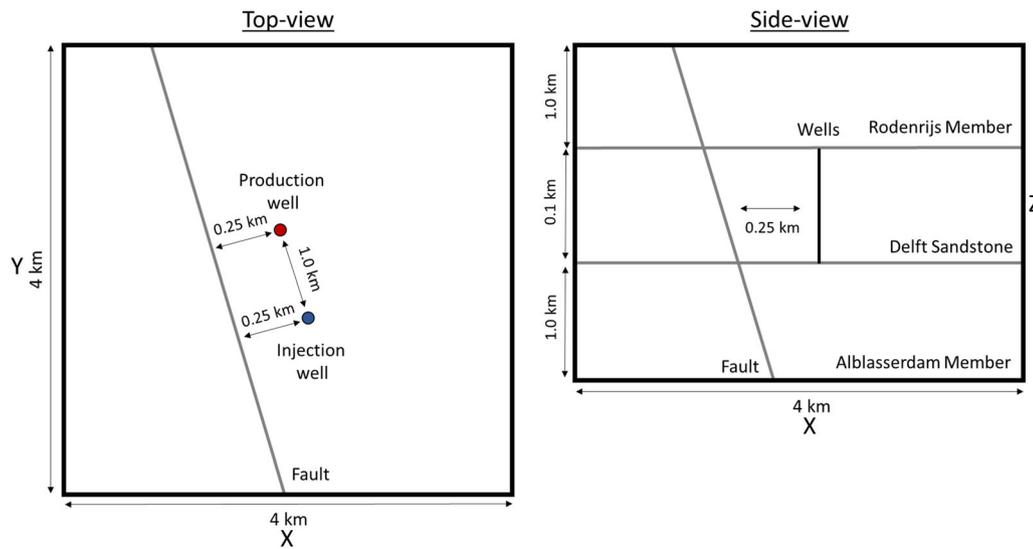
Figure 3. Top (left) and side (right) view of the Delft sandstone model (not to scale).

Table 5. Mechanical, thermal and hydraulic properties of geological units and the fault in the Delft sandstone base case model.

Model property	Rodenrijs member (claystone)	Delft sandstone member	Albalasserdam member (sst/clst)	Fault
Young's modulus (GPa)	40	15	25	15
Poisson's ratio (-)	0.2	0.2	0.2	0.2
Solid bulk modulus (GPa)	50	60	45	60
Drained bulk modulus (GPa)	22.2	8.33	13.9	8.33
Biot coefficient (-)	0.56	0.86	0.69	0.86
Friction coefficient (-)	–	–	–	0.6
Cohesion (MPa)	–	–	–	0
Solid thermal conductivity (W/m/°C)	2.0	4.5	2.5	4.5
Solid heat capacity (J/kg/°C)	950	730	860	730
Volumetric bulk thermal expansion coefficient (1e-6/°C)	30	30	30	30
Solid density (kg/m³)	2650	2650	2650	2650
Hor. permeability (mD)	1	1000	1	100
Hor./vert. permeability (-)	1	2	1	1
Porosity (%)	10	20	10	20

wells are vertical and intersect the entire Delft sandstone reservoir. They are assumed to be open to flow along the entire well path inside the reservoir formation.

The same geometry is used as for the Slochteren model (Fig. 3). The top layer was artificially extended to 1000 m to avoid boundary effects in the model, thus integrating all overlaying formations as well. The thickness of the Alblasserdam member varies significantly between <100 m and >1300 m. A thickness of 1000 m is chosen as representative for the bottom layer. The same temperature, pressure and stress gradients as well as heat flow values are used as in the Slochteren model. The same operational and wellbore data were used in the Delft sandstone model as in the Slochteren sandstone model. Variations in other model properties are described below (Table 5).

Rock matrix, fault and fluid properties

No consistent literature values were found for Rodenrijs, Delft sandstone and Alblasserdam. Therefore, the values from the Slochteren model were used for Sandstone and Claystone. For the Alblasserdam member approximately average values between Rodenrijs member and Delft Sandstone member were used.

Compared to the Slochteren reservoir, the Delft sandstone member has a higher permeability. The top and bottom layers have a higher porosity. Thermophysical properties of the Delft sandstone layer were based on the Slochteren sandstone model and adapted based on Willems et al. (2020). Rodenrijs properties were based on the claystone properties from the Slochteren model and Alblasserdam properties were based on a mix between sandstone and claystone properties with specific information taken
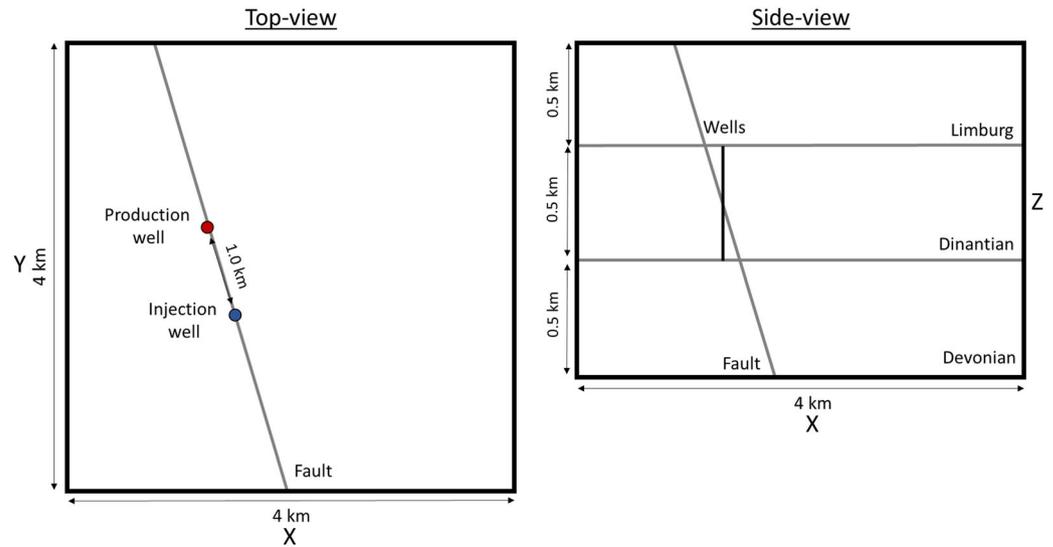
Figure 4. Top (left) and side (right) view of the Dinantian limestone fault model (not to scale).

from Willems et al. (2020). For the Delft sandstone model, the same fault properties as in the Slochteren sandstone model were used. Due to the lack of reservoir fluid data, we assume pure water as representative reservoir fluid for the Delft sandstone model.

Besides the base case Delft sandstone model, a small sensitivity analysis is performed for re-injection temperature and well-to-fault distance.

Dinantian limestone reservoir models

The Dinantian carbonate formation is the deepest formation we consider in our analysis. Here, we simplify the geology to a horizontal Limburg claystone layer as top seal, a horizontal Dinantian limestone layer as reservoir layer and a horizontal Devonian claystone-sandstone layer as bottom seal. Due to the low permeability of the rock matrix, we consider three models for geothermal exploitation of the Dinantian limestone: (a) wells intersect a high permeability fault ('Dinantian fault model'), (b) wells intersect a fault zone ('Dinantian fault damage zone model') and (c) hydraulically fractured parallel horizontal wells are drilled next to the fault representing a multi-stage EGS ('Dinantian EGS model').

Model geometry and boundary conditions

The depth of the Dinantian varies between 2 and 9 km. For the considered Ultra Deep Geothermal development with temperatures >120°C, we use a 4.5 km deep Dinantian reservoir top. A thickness of 500 m is assumed. The same thickness is used for the top and bottom layers. Fault geometry and properties are the same as in the Slochteren model. All stress, pressure and temperature initial and boundary conditions are the same as in the Slochteren model adapted for the depth.

Operational and wellbore data is the same as in the other two models except that for one scenario, the two deviated wells are 1000 m apart and intersect the fault, and in another scenario two horizontal wells parallel to the minimum horizontal stress direction are 500 m apart and hydraulically connected by five hydraulic fractures with a spacing of 200 m. The distance between wells and fault is here 250 m.

Three models are setup for the Dinantian reservoir. Due to the low reservoir permeability geothermal exploitation needs to focus on existing fault zones (Scenarios S37 and S38) or stimulated

fractures (Scenario S39). Figures 4, 5 and 6 display the geometries of the Dinantian limestone reservoir models.

Rock matrix, fault and fluid properties

The description of the Limburg properties can be found in the respective sections on the Slochteren model. The Devonian properties are an approximate average of claystone and sandstone and thus correspond to the Alblasserdam Member as defined above for the Delft model. For the Dinantian, typical values for limestone were used when no specific reservoir information was available (Table 6).

Geomechanical rock properties. For the Dinantian limestone, a Young's modulus of 40 GPa and a Poisson's ratio of 0.2 were used according to the value for the Carboniferous in Lele et al. (2015). According to Schmitt (2015), the solid bulk moduli of Calcite and Dolomite are 73.3 GPa and 94.9 GPa, respectively. Assuming a calcite dominated limestone, we use a value of 80 GPa. The resulting drained bulk modulus and Biot coefficient are 22.2 GPa and 0.72, respectively.

Hydraulic rock properties. The Dinantian is a low porosity and low permeability limestone formation. Similar or even lower values can be expected for the top and bottom layers. Flow is governed by fracture flow.

Thermophysical rock properties. According to Fuchs et al. (2015), Calcite and Dolomite have a thermal conductivity of 3.4 and 5.4 W/m/°C, a heat capacity of 820 and 870 J/kg/°C and a density of 2710 and 2880 kg/m³, respectively. We use values closer to the ones of calcite. Srinivasan (1955) reports similar values of thermal expansion coefficient for calcite and for quartz. Therefore, we use the same value of 30 1e-6/°C for the Dinantian limestone and for the Slochteren sandstone.

Fault and fracture properties. Fracture aperture, based on FMI logs in the Dinantian carbonates, were approximately 110 µm (Broothaers et al., 2019; Van Leverink & Geel, 2019). Assuming this fracture aperture to be equivalent to the hydraulic aperture, the cubic law yields a fracture permeability of 1000 mD. Thus, we use the same fault properties as in the Slochteren model except for a
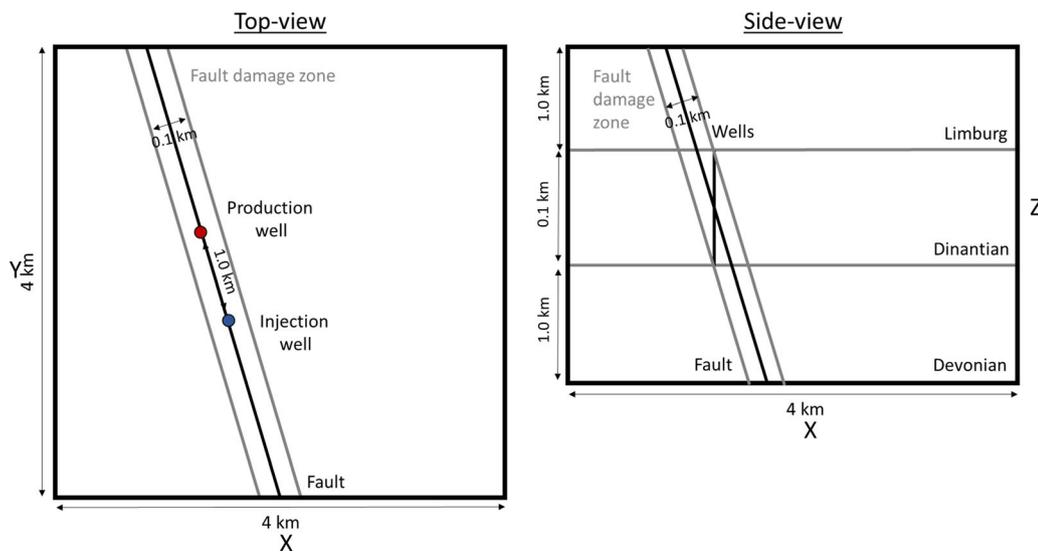
Figure 5. Top (left) and side (right) view of the Dinantian fault damage zone model (not to scale).
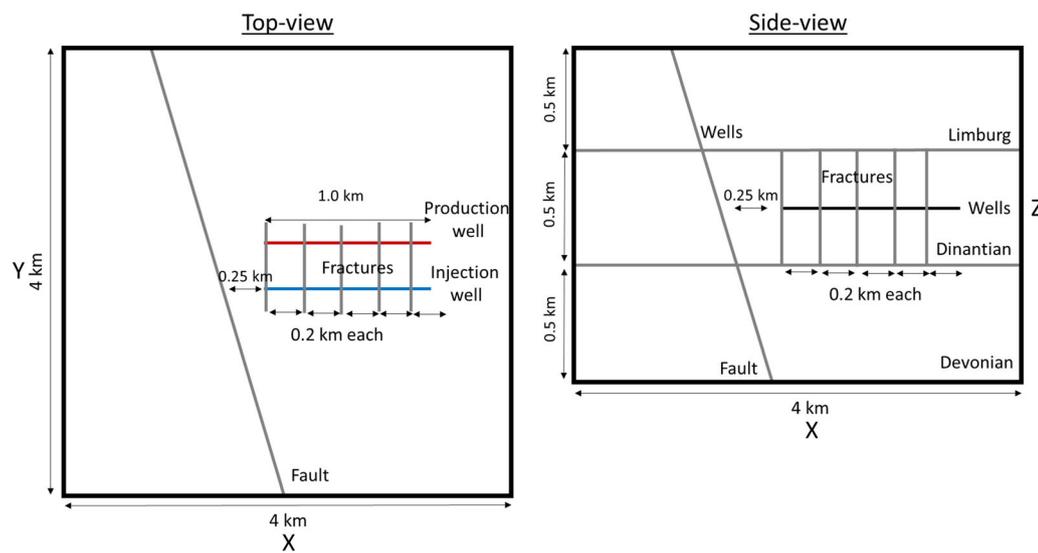
Figure 6. Top (left) and side (right) view of the Dinantian EGS model (not to scale).

higher fault permeability of 1000 mD, a correspondingly higher aperture of 110e-6 m and a higher fault porosity of 100%. The same parameters were used for hydraulic fractures.

Reservoir fluid properties. No fluid information is available for the deep Dinantian limestone formation. We thus use high salinity fluid of the Groß Schönebeck reservoir as formation fluid. This is the same as in the Slochteren model.

Results

Slochteren sandstone

Base case model
With the base case model geometry and parameters, the model showed a potential fault failure after 11.45 years of cold-water injection when the maximum slip tendency on the fault reaches the critical value of 0.6 (Fig. 7). Figure 8 shows the temperature and pressure contours around the injection well and the slip tendency on the fault plane after 30 years of circulation. The slip tendency values increase systematically when the cold thermal front reaches the fault plane. The pressure perturbation due to the injection process on the other hand stabilizes relatively quickly and does play only a secondary role in the slip tendency on the fault plane. Figure 9 illustrates the initial and final absolute stresses, thermal stress, pore-pressure and temperature along x-axis and z-axis across the injection well after 30 years of geothermal operation. The figure shows an increased thermal stresses at the formation boundaries. This occurs due to the higher rock stiffness of the top and the bottom layers. It can also be observed from Fig. 9 that the maximum pore-pressure increase around the injection well is 3.8 MPa. The temperature around the injection well reaches the injection water temperature, that is, 30°C. Thermal stresses generated due to the temperature change affect the mechanical

Table 6. Mechanical, thermal and hydraulic properties of geological units and the fault/fractures in the Dinantian limestone base case model.

Model property	Limburg (claystone)	Dnantian (limestone)	Devonian (clst/sst)	Fault/fractures
Young's modulus (GPa)	40	40	25	40
Poisson's ratio (-)	0.2	0.2	0.2	0.2
Solid bulk modulus (GPa)	50	80	45	80
Drained bulk modulus (GPa)	22.2	22.2	13.9	22.2
Biot coefficient (-)	0.56	0.72	0.69	0.69
Friction coefficient (-)	–	–	–	0.6
Cohesion (MPa)	–	–	–	0
Solid thermal conductivity (W/m/°C)	2.0	3.5	2.5	3.5
Solid heat capacity (J/kg/°C)	860	830	860	830
Volumetric bulk thermal expansion coefficient (1e-6/°C)	30	30	30	30
Solid density (kg/m^3)	2650	2750	2650	2750
Hor. permeability (mD)	0.001	1	0.001	1000
Hor./vert. permeability (-)	1	1	1	1
Porosity (%)	1	2	1	100
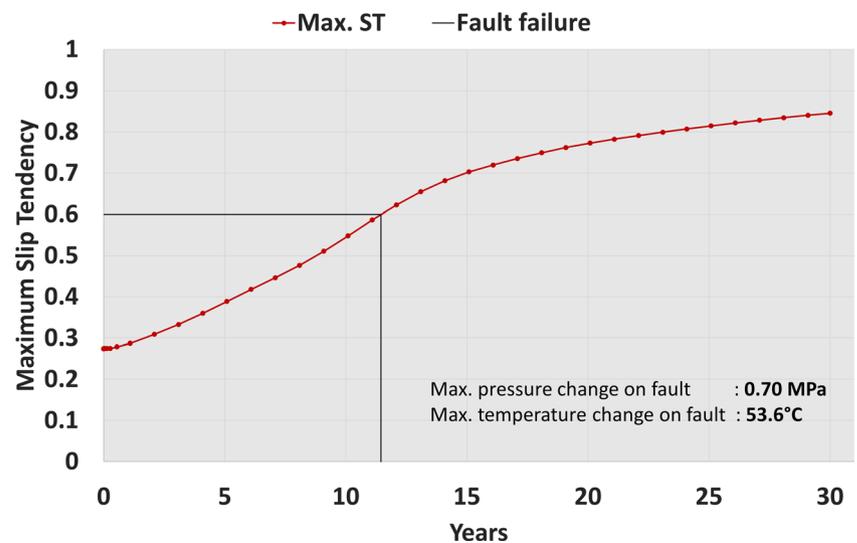
Figure 7. Maximum slip tendency on the fault and fault failure within the reservoir unit of the Slochteren base case model.

stress state of the rocks. The combined effect of the thermal, hydraulic and mechanical processes results in an increase in the computed slip tendency along the fault. After 30 years of cold water injection, ~0.077 km² fault area undergoes failure and the fault plane within the reservoir section experiences a maximum slip tendency of 0.85.

Sensitivity analysis
To understand the impact of the most important reservoir geometries, geological and operational parameters, a sensitivity analysis was performed (Table 7). The results obtained from the sensitivity analysis cases were only analysed in the reservoir section to ensure the same initial stress state. Figure 10 shows that the parameters that constitute the thermal and mechanical governing equations have the highest impact on the fault failure potential. These parameters included the stress gradients; geo-mechanical

reservoir properties like Young's modulus and Poisson's ratio; operational and wellbore data such as the distance between the wells and the fault, re-injection temperature, flow rate; other geological properties like temperature and pressure gradients, thermal expansion coefficient, fault dip, reservoir depth and porosity of the reservoir rock. Many of these parameters also impacted the magnitudes of maximum temperature change along the fault (Fig. 11). This indicates a strong correlation between the thermal stresses and the computed slip tendency values as dictated by Equation (3). However, such correlation was not observed with the maximum change in pressure values given in Fig. 12. Parameters such as pore-pressure differential, permeability and fluid viscosity did exert only a minor impact on the slip tendency of the fault, indicating how the hydraulic feedback coupling is not significant to determine the fault failure mechanism. A cross examination of Figs. 10 and 13 indicates that the cases with higher
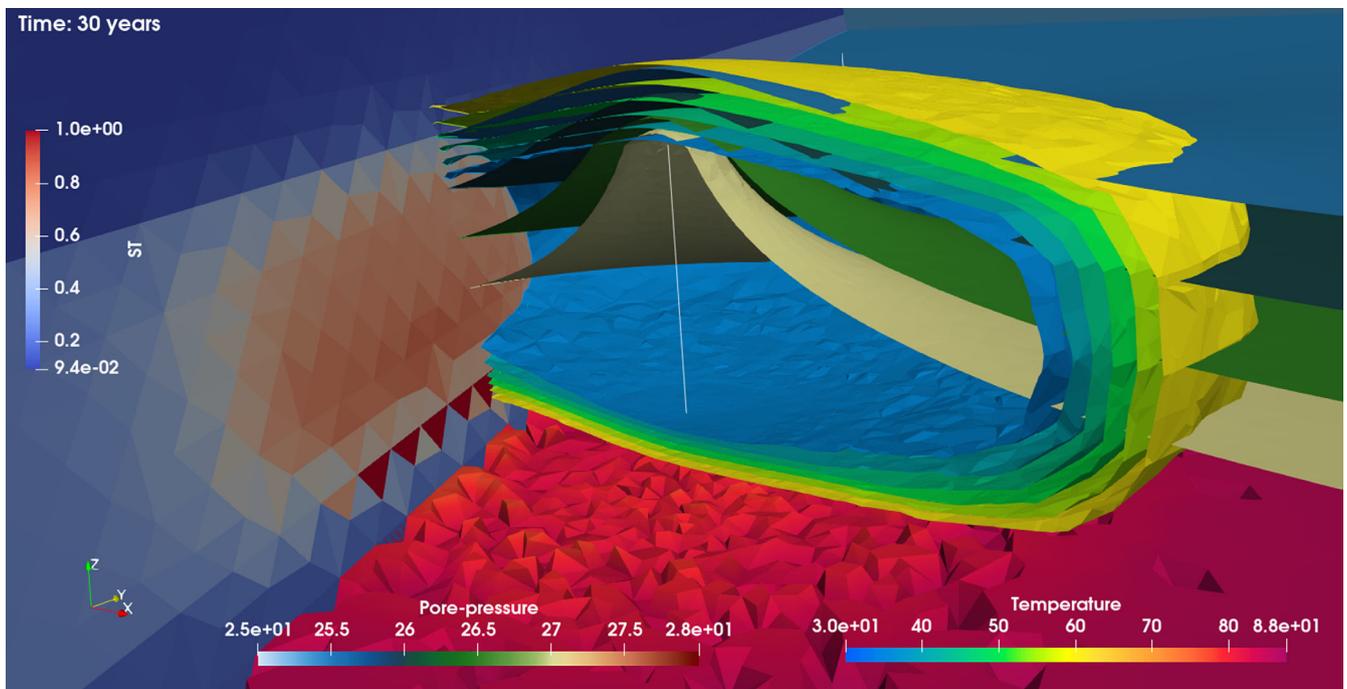
Figure 8. Temperature contours (in °C), pressure contours (in MPa) and slip tendency (unitless) on the fault in the Slochteren base case model after 30 years of circulation.
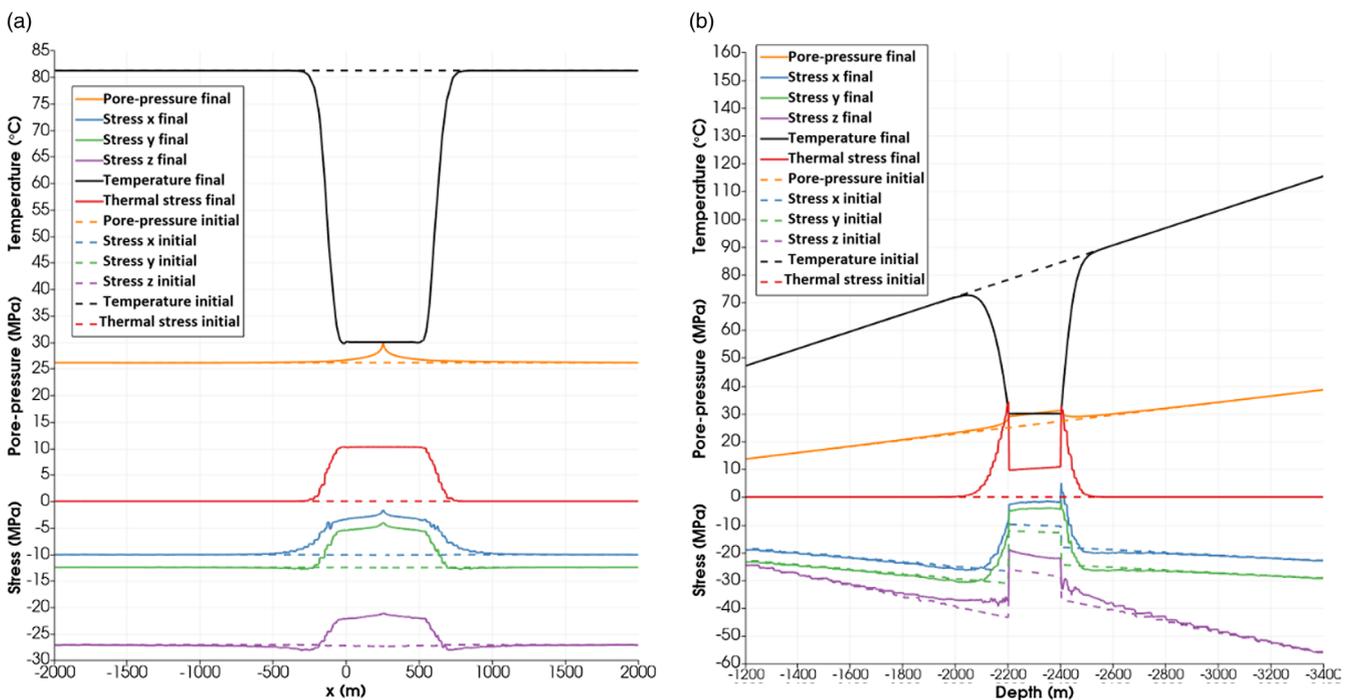
Figure 9. Temperature, pore-pressure and effective stresses (compression is negative) across the injection well (a) along x-axis and (b) along z-axis, initial (dash) and after 30 years (solid) of circulation in the Slochteren base case model.

slip tendencies also resulted in a larger area of the fault with a potential to fail. Even by assuming the same amount of slip for the two cases, a larger area would result in a larger seismic moment and therefore in a higher magnitude of the potential induced event

assuming that the slip would be seismic. Figure 14 shows that these cases also failed earlier than the cases with low slip tendency values.

One simulation scenario was considered without thermo-elastic effects which resulted in a significant change in the slip tendency

Table 7. Modelling scenarios for the Slochteren sandstone, Delft sandstone and Dinantian limestone sensitivity analysis.

Category	Case ID	Changed parameter	Changed values
	S1	Base case scenario	–
Geometry	S2a,b	Depth of reservoir top	1500 m, 3000 m
	S3a,b	Reservoir thickness	100 m, 250 m
	S4	Fault strike	N150°E
	S5a,b,c	Fault dip	60°, 70°, 85°
Geomechanical properties of reservoir	S6a,b	Young's modulus	3 GPa, 30 GPa
	S7a,b	Poisson's ratio	0.1, 0.25
	S8a,b	Biot's coefficient	0.5, 0.97
Hydraulic properties of reservoir	S9a,b	Hor. permeability	50 mD, 350 mD
	S10a,b	Hor./vert. permeability ratio	1, 10
	S11a,b	Porosity	10%, 30%
Thermophysical properties of reservoir	S12a,b	Thermal conductivity	3 W/m/°C, 7.7 W/m/°C
	S13a,b	Heat capacity	650 J/kg/°C, 1050 J/kg/°C
	S14a,b	Bulk thermal expansion coefficient	20e-6 1/°C, 40e-6 1/°C
Fault properties	S15a,b	Fault permeability, porosity	0 D, 0%; 10 D, 100%
Temperature, pressure, stress gradients	S16a,b	Geothermal gradient	20°C/km + 10°C, 40°C/km + 10°C
	S17a,b	Pressure gradient	10 MPa/km, 12 MPa/km
	S18a,b	Vertical stress gradient	21 MPa/km, 23 MPa/km
	S19a,b	Maximum horizontal stress gradient	15 MPa/km, 23 MPa/km
	S20a,b	Minimum horizontal stress gradient	13 MPa/km, 23 MPa/km
	S21a,b	Maximum horizontal stress direction	N150°E, N170°E
Reservoir fluid parameters	S22a,b	Density	980 kg/m³, 1200 kg/m³
	S23a,b	Viscosity	0.3 mPas, 1.5 mPas
	S24a,b	Specific heat capacity	3200 J/kg/°C, 4200 J/kg/°C
	S25a,b	Thermal conductivity	0.6 W/m/K, 0.7 W/m/K
	S26a,b	Bulk modulus	2 GPa, 4 GPa
Operational and wellbore data	S27a,b	Well spacing	500 m, 1500 m
	S28a,b	Re-injection temperature	15°C, 45°C
	S29a,b	Flow rate	30 l/s, 100 l/s
	S30a,b,c	Well to fault distance	0 m, 500 m, 1000 m
Thermoelastic effect	S31	Thermal expansion coefficient	0
Special scenarios	S32	Deep low porosity reservoir	$D = 3000$ m, $H = 100$ m, $k = 100$ mD, $T = 10$ Dm, kh/kv = 10, $\phi = 10\%$, $\alpha = 0.5$, $E = 30$ GPa, $\upsilon = 0.1$, $q = 40$ l/s
	S33	Shallow high porosity reservoir	$D = 1500$ m, $H = 250$ m, $k = 200$ mD, $T = 50$ Dm, kh/kv = 1, $\phi = 30\%$, $\alpha = 0.97$, $E = 3$ GPa, $\upsilon = 0.25$, $q = 100$ l/s
Delft Sandstone model	S34	Base case scenario	–
	S35a,b	Re-injection temperature	15°C, 45°C
	S36a	Well-to-fault distance	500 m
Dinantian Limestone model	S37	Base case fault model	–
	S38	Damage zone model	50 m fault damage zone
	S39a,b	EGS model	Wells 250 m, 500 m from fault

MAXIMUM SLIP TENDENCY ON FAULT
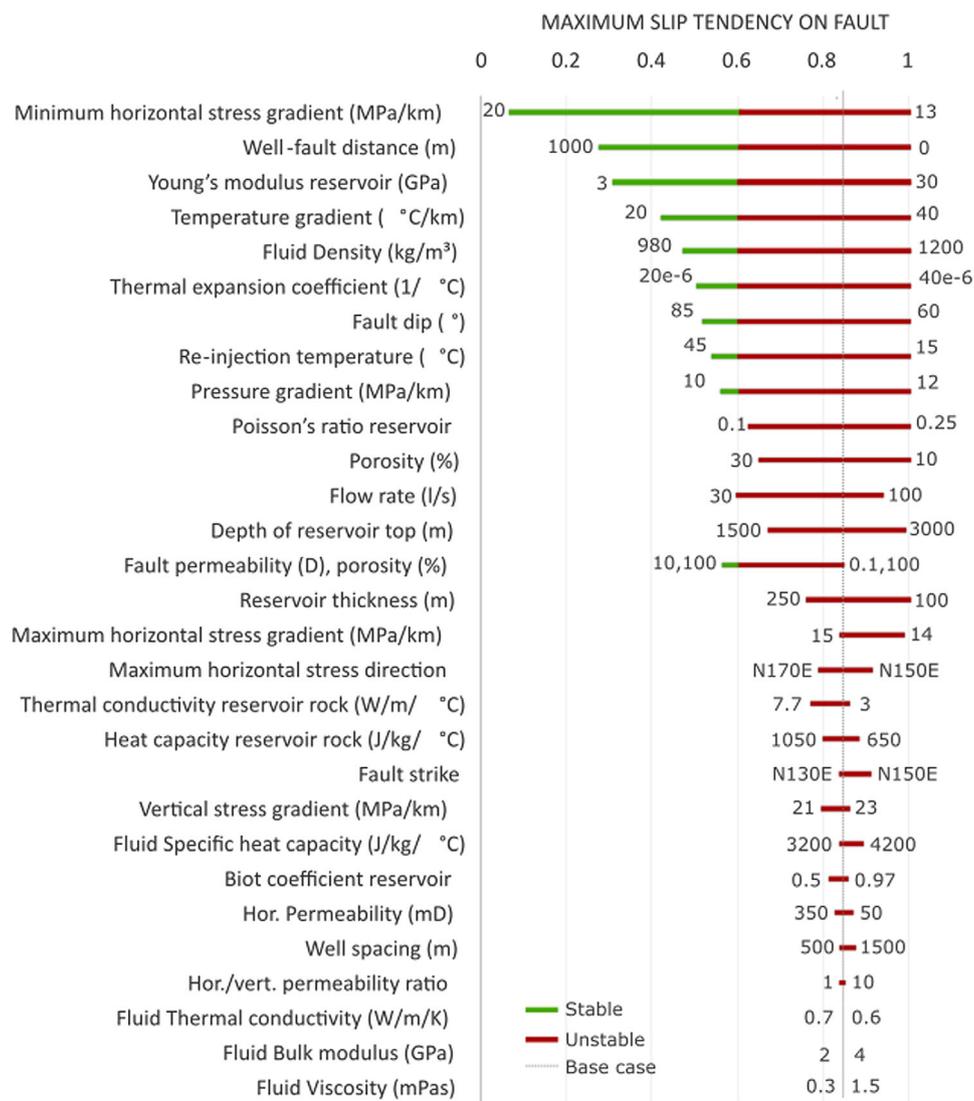
Figure 10. Results of the sensitivity analysis for the fault within the reservoir unit: Maximum slip tendency after 30 years of circulation in the Slochteren models.

on the fault plane. The maximum slip tendency without thermo-elastic effects is only 0.27 instead of 0.85, highlighting the importance of thermal effects on slip tendency in our models. Two special case scenarios were also simulated: (a) a deep low porosity reservoir model and (b) a shallow high porosity reservoir model. The maximum slip tendencies observed in the reservoir layer in these cases after 30 years of geothermal operation were 0.7 and 0.4, respectively, indicating that deep low porosity reservoirs have a higher fault slip potential compared to shallow high porosity reservoirs.

Delft sandstone

Base case model
The Delft sandstone reservoir shows a potential fault failure after 3.95 years of cold-water injection. With 30 years of geothermal operation, the fault plane within the reservoir section experiences a maximum slip tendency of 1 and a fault area of 0.091 km^2 potentially undergoes failure. The maximum change in the temperature at the fault section within reservoir unit is 54.2°C. As compared to the Slochteren sandstone base case model, the Delft sandstone model experienced a higher slip tendency and a quicker fault failure (Table 8). This can be attributed to the difference in the geometry of the two models. A smaller reservoir thickness of the Delft reservoir leads to a wider distribution of the thermal front.

Sensitivity analysis
A sensitivity analysis was performed for different re-injection fluid temperatures: (a) 15°C, (b) 30°C (base case) and (c) 45°C. With 15°C re-injection temperature, the rock matrix experiences higher thermal stresses as compared to the base case and thus fault failure occurs earlier at 3.15 years. The change in temperature at the fault surface after 30 years is 69.6°C with a failure area of 0.10 km^2. The scenario with re-injection water temperature of 45°C, on the other hand, experiences lower thermal stresses as compared to the base case. The fault failure occurs after 6.45 years. The maximum

MAXIMUM TEMPERATURE CHANGE ON FAULT (°C)

	0	20	40	60	80

Parameter		
Well-fault distance (m)	1000 ———————————— 0	
Temperature gradient (°C/km)	20 ————————— 40	
Depth of reservoir top (m)	1500 ——————————— 3000	
Re-injection temperature (°C)	45 ————————— 15	
Fault permeability (D), porosity (%)	0,0 —————————— 10,100	
Flow rate (l/s)	30 ——— 100	
Thermal conductivity reservoir rock (W/m/ °C)	7.7 — 3	
Reservoir thickness (m)	100 — 250	
Maximum horizontal stress direction	N150°E — N170°E	
Fault dip (°)	85 — 60	
Porosity (%)	10 — 30	
Fluid Specific heat capacity (J/kg/ °C)	3200 — 4200	
Fault strike	N150°E — N130°E	
Well spacing (m)	1500 — 500	
Heat capacity reservoir rock (J/kg/ °C)	650 ¦ 1050	
Hor./vert. permeability ratio	10 ¦ 2	
Fluid Density (kg/m³)	980 ¦ 1200	
Pressure gradient (MPa/km)	10 ¦ 12	
Fluid Thermal conductivity (W/m/K)	0.7 ¦ 0.6	
Fluid Viscosity (mPas)	0.3 ¦ 1.5	
Hor. Permeability (mD)	350 ¦ 50	
Young's modulus reservoir (GPa)	3 ¦ 30	
Poisson's ratio reservoir	0.1 ¦ 0.25	
Biot coefficient reservoir	0.5 ¦ 0.97	
Thermal expansion coefficient (1/ °C)	20e-6 ¦ 40e-6	
Vertical stress gradient (MPa/km)	21 ¦ 23	
Maximum horizontal stress gradient (MPa/km)	14 ¦ 20	
Minimum horizontal stress gradient (MPa/km)	13 ¦ 20	
Fluid Bulk modulus (GPa)	2 ¦ 4	

-------- Base case

Figure 11. Results of the sensitivity analysis for the fault within the reservoir unit: Maximum temperature change after 30 years of circulation in the Slochteren models.

temperature change on the fault plane after 30 years is 38.8°C, and the critically stressed fault area is 0.056 km^2.

In another sensitivity analysis scenario, the distance between the injection well and the fault was increased to 500 m. In this case, the fault failure was not observed within the operational period of 30 years. The maximum slip tendency was observed to be 0.51, the maximum temperature change on the fault to be 84.4°C and the maximum pressure change on the fault was 84.1 MPa.

Dinantian limestone

Fault-dominated exploitation
In the Dinantian base case model and the Dinantian damage zone model, the injection and production wells intersect the fault. In both the cases, fault failure is observed at the beginning of circulation. Figure 15 shows the cross-sections across the injection wells in each case. The injection water flows outwards into the reservoir unit in the base case model, whereas in the damage zone model, the cold injection water flows primarily through the fault damage zone also intersecting the top and bottom units.

Enhanced Geothermal Systems (EGS)
As compared to the fault-dominated exploitation of the Dinantian limestone reservoir, the EGS models shows significantly lower potential of fault failure. The injected water in the EGS models is distributed into the reservoir unit through the hydraulic fractures. As a result, the temperature changes primarily affect the immediate vicinity of the injection well and have little impact on the stress changes occurring on the fault plane. Figure 16 shows the slip tendency on the fault plane in the EGS models after 30 years of circulation. The EGS system with 500 m distance between injection well and the fault shows no failure potential, whereas the EGS model with 250 m distance between the injection well and the fault shows failure potential after 28.7 years.
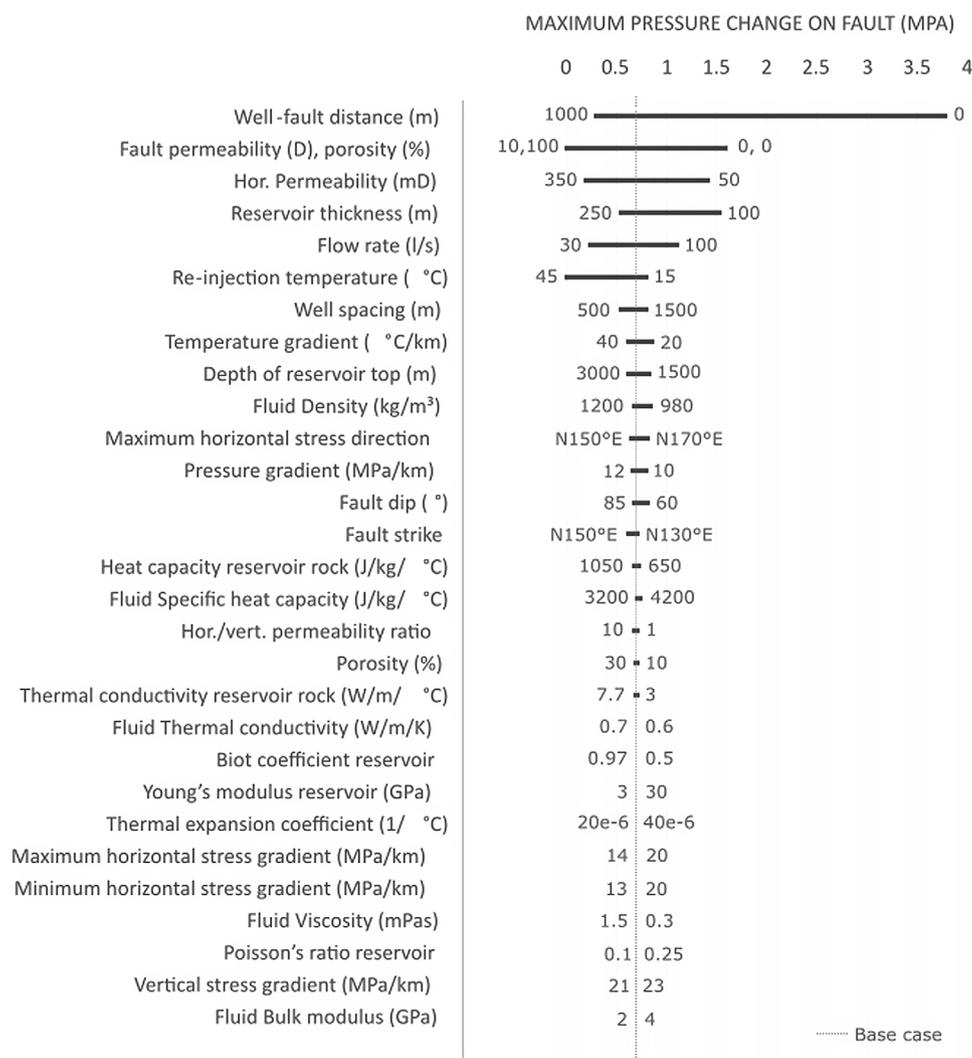
Figure 12. Results of the sensitivity analysis for the fault within the reservoir unit: Maximum pore-pressure change after 30 years of circulation in the Slochteren models.

Discussion

The study suggests that for the given assumptions and boundary conditions, the changes in the slip tendency of a fault (2D planar discontinuity with zero cohesion) can largely be attributed to thermo-mechanical effects. Once a new equilibrium is reached in a doublet system after a few months, the direct influence of pore pressure on slip tendency remains constant, while the cold-water front will continue to expand around the injection well for as long as the well is in operation. A significant increase in the slip tendency was observed when this low temperature front reached the fault zone. Besides the obvious importance of the stress field and the local fault geometry, rock mechanical properties and operating conditions have a major influence on the induced stress changes and the related fault activation potential triggered by geothermal operations. Thus, careful selection of a suitable target formation and the operational parameters is crucial to minimize the risk of induced seismicity. The most important geological parameters that should be known while selecting the geothermal site are the regional stress gradients, temperature gradient, pressure gradient, geo-mechanical properties of the reservoir layer such as the Young's modulus and Poisson's ratio, thermal expansion coefficient of the formation, fault orientation, reservoir porosity, depth and thickness of the reservoir layer. Lower stress, temperature and pressure gradients, lower reservoir rock stiffness, shallower depth, higher reservoir porosity, larger reservoir thickness, lower thermal expansion coefficient and higher fault dip contribute to a low risk geothermal environment. Besides selecting a low-risk geothermal formation, the failure potential can further be minimized by optimizing operational parameters. The key planning and operational parameters to be considered include the distance between the injection well and existing known faults, re-injection temperature and injection flow rate. During the geothermal operations, the most effective measures to reduce the risk of induced seismicity are increasing the re-injection temperature and decreasing the injection rate. The EGS system with optimized well-to-fault distance can be an effective technique for the mitigation of induced seismicity in deeper reservoirs such as Dinantian limestone.
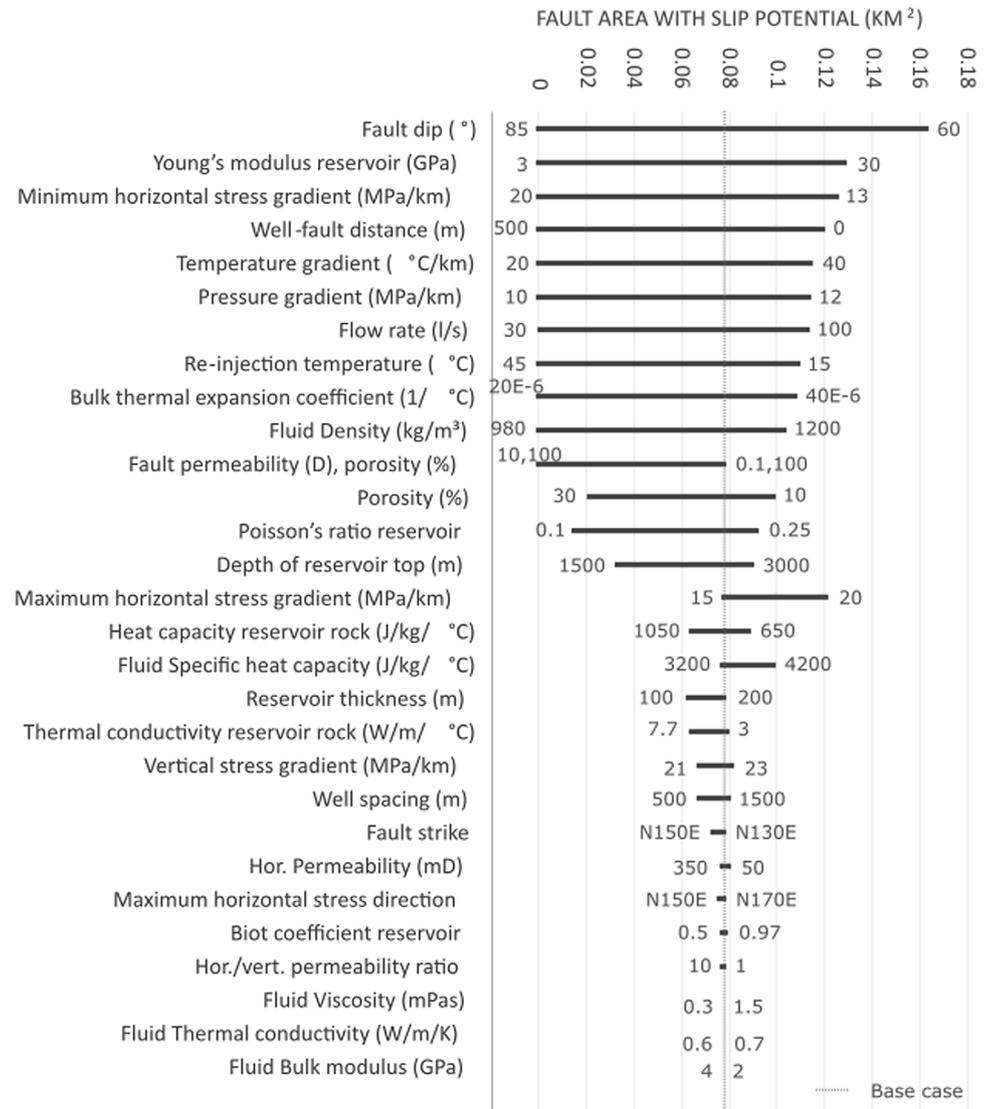
FAULT AREA WITH SLIP POTENTIAL (KM²)

In this study, we did not consider fault offsets to avoid further complexity in the interpretation of the results and numerical artefacts in the form of stress concentrations on sharp geometrical edges, which are not found in reality, as described before. With a fault offset of less than 200 m (hydraulic connection between reservoir formation on both sides of the fault), the effect would be similar to the results of the sensitivity analysis of the reservoir thickness. Within the 0–200 m range, a larger fault offset would lead to a pressure increase and temperature reduction on the fault, leading to earlier fault slip and increasing slip tendencies. With larger fault offsets, the impermeable Limburg claystone formation on the other side of the fault would prevent flow and convective heat transfer across the fault, leading to higher pressures, but significantly less temperature changes on the fault and thus significantly lower slip tendencies. This case would thus be similar to the impermeable fault scenario.

We note again that although the slip tendency may indicate fault reactivation, it does not tell anything about the seismicity to be expected from this fault failure. Therefore, we performed an additional analysis by applying the rate-and-state friction (RSF) formalism to the same model to get some information about the dynamics of a potential fault slip (Supplementary material S1). The empirical constants describing the frictional properties of the fault in the RSF framework were taken from Hunfeld et al. (2017). The RSF parameters provided in the cited study were determined by direct shear experiments performed on simulated Slochteren sandstone fault gouges. These experiments did not include fluid injection and did not consider the effect of long-term thermal stressing of the samples. Nevertheless, based on Hunfeld et al. (2017), the Slochteren sandstone fault gouges show velocity strengthening behaviour in the direct shear experiments, and consequently our RSF model also resulted in slow, stable slip, which might be an indicator for aseismic slip (Guglielmi et al., 2015). Hunfeld et al. (2017) have also indicated that the overlying Zechstein formation shows velocity weakening characteristics. Since in our model the pore pressure and cooling-induced stress
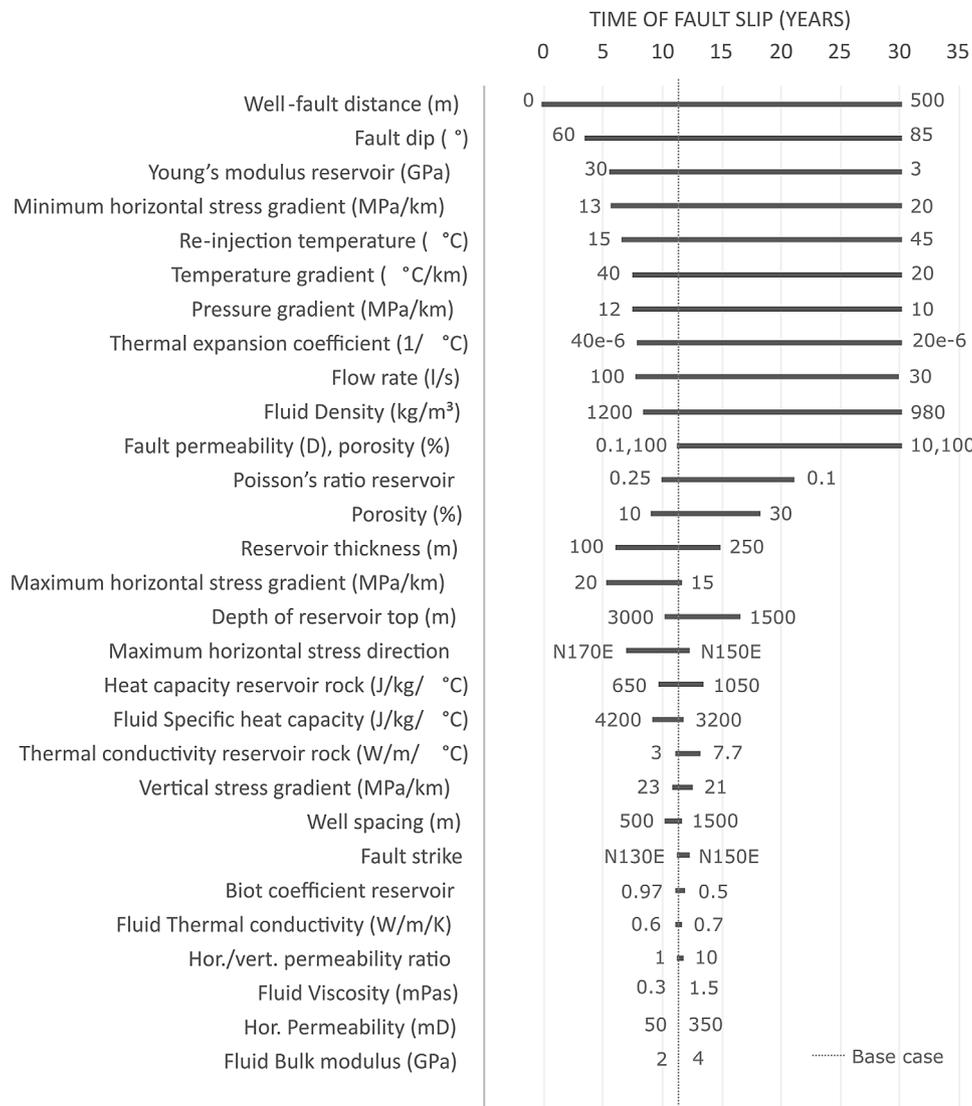
Figure 14. Results of the sensitivity analysis for the fault within the reservoir unit: Time to reach the critical slip tendency in the Slochteren models.

Table 8. Comparison of Slochteren, Delft and Dinantian EGS models.

	Slochteren	Delft	Dinantian EGS
Max ST on fault (in reservoir unit)	0.85	1.0	0.61
Max temperature change on fault (°C)	53.6	54.2	0.89
Max pressure change on fault (MPa)	0.70	0.16	4.7
Area of fault with ST > μ (km²)	0.077	0.09	0.0013
Time until ST > μ (years)	11.45	3.95	28.7

changes are mainly limited to the fault area overlapping with the reservoir layer (see Fig. 8), we neglected the potentially different friction behaviour of the Zechstein caprock and characterized the entire fault with a single parameter set. This choice is justified by the fact that no significant seismicity (i.e. $M_w > 2$) is observed in the hydrothermal systems of the Netherlands and the velocity strengthening behaviour of the faults in these reservoirs could be one potential reason for this. Nevertheless, faults in the Netherlands may also exhibit velocity weakening behaviour and adapting the RSF parameters in our model accordingly would lead to seismic rather than a seismic slip. A thorough analysis of the frictional behaviour of reactivating faults in the Slochteren

(a)

(b)
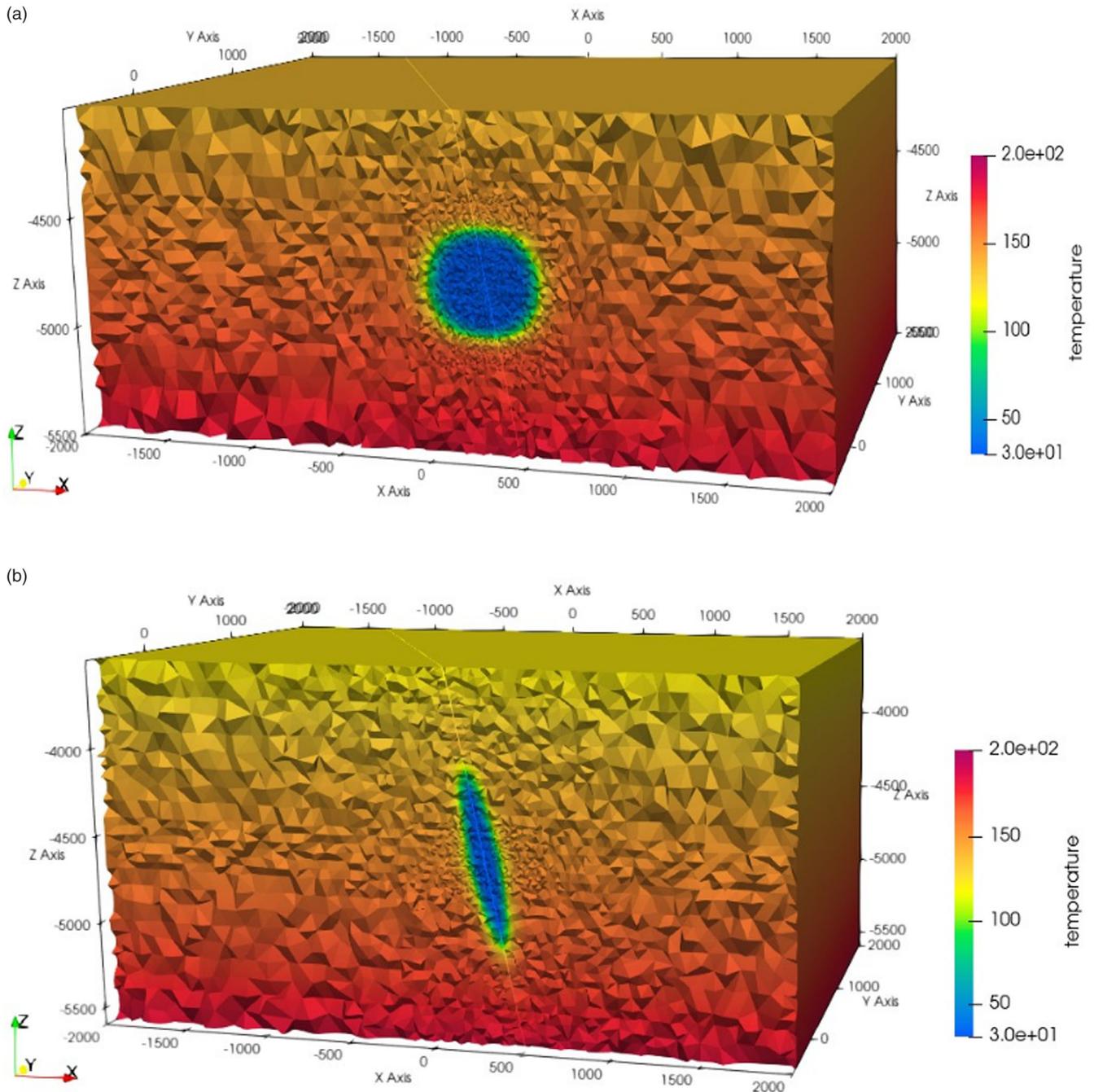
Figure 15. Comparison of temperature distribution after 30 years of circulation in the (a) Dinantian fault model and (b) the Dinantian damage zone model.

Sandstone formation (related to geothermal operation) has to be the subject of future studies based on field observation and site-specific geological models.

A limitation of the current model is the lack of validation with field observations from the Netherlands due to the lack of data. No induced seismicity has been observed in the conventional matrix-type geothermal reservoirs in the Netherlands, whereas a previously observed induced seismicity in the Dinantian limestone reservoir indicates the need of a detailed analysis of the geological and operational settings of EGS systems.

We note that we have chosen a simplified approach to include the Zechstein formation in our simulations by modelling it as a homogeneous linear elastic layer without considering secondary creep mechanism. This was done intentionally to avoid further model complexity since this study focuses mainly on the fluid injection induced seismicity inside the respective reservoir layers. In addition, considering the Zechstein formation as a homogeneous viscoelastic layer that consists of pure rock salt would also be a similarly strong assumption. However, it was shown in the case of the Groningen gas field that the presence

(a)

(b)
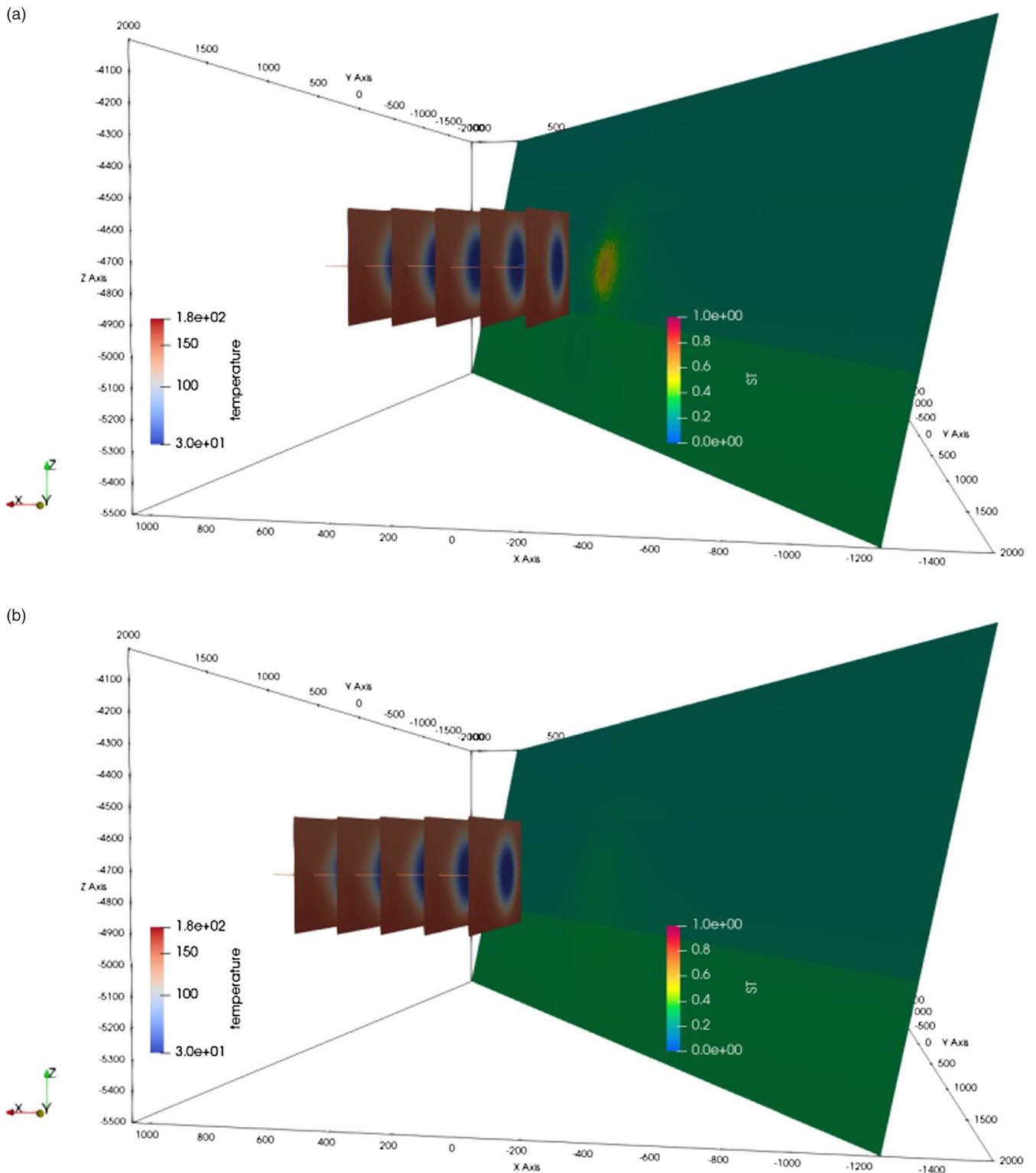
Figure 16. Comparison of temperature distribution on hydraulic fractures and slip tendency on the fault after 30 years of circulation in (a) the Dinantian EGS model with 250 m well-fault spacing and (b) 500 m well-fault spacing.

of the viscoelastic Zechstein caprock can contribute to depletion-induced seismic slip (Wassing et al., 2017; Candela et al., 2019).

Therefore, the absolute values for slip tendency, failure area, temperature and pressure should be interpreted considering the limitations and assumptions of our model. Nevertheless, the absolute values demonstrate how the calculated slip tendency for this model changes when the input parameters are changed within realistic ranges that apply to the Netherlands.

Potential future studies can include site-specific model geometries, further refined meshes, a nonlinear failure criterion, poro-elastic coupling and a creep constitutive law for the Zechstein salt. It has to be noted that implementing more realistic fault systems (e.g. en echelon segmented) will have a major impact on the individual interplay of key impact factors and resulting slip and induced seismicity patches along the fault.

Conclusions

Our results of Dutch geothermal well doublet THM models indicate that thermal effects can play a major role in fault stability, supporting the observations of recent numerical modelling studies (Wassing et al., 2021; Kivi et al., 2022). Cooling-induced thermal stresses cause tensile stresses, thereby reducing the magnitude of the resulting compressive stresses. This increases the slip tendency of the fault. Thermal stresses are highly sensitive to geo-mechanical reservoir rock properties, for example, Young's modulus and Poisson's ratio. The higher the rock stiffness, the higher the chances of failure during cold fluid injection. Within the range of investigated geometries, the Slochteren sandstone exhibits a more stable fault configuration when characterised by a higher fault dip and a fault strike that is oriented at a greater angle relative to the SHmax direction. According to the sensitivity analysis, a significant variation in stress gradients across different principal directions corresponds to elevated shear stresses, which increases the potential for fault failure. Among the thermal properties, bulk thermal expansion coefficient has the most significant effect on fault stability. Well-to-fault distance, re-injection temperature and injection flow rate are key parameters that can influence the seismic risk. Therefore, it is essential to carefully consider these parameters when planning a geothermal system. In the case of typical Slochteren deep geothermal systems, hydraulic parameters and fluid properties such as rock permeability, fluid viscosity and fluid density have minor impact on fault stability within their respective investigated ranges.

Authors' contributions. BM set up and carried out all simulations presented in the manuscript. HH gathered and compiled the reservoir and fluid data and supervised the study, MC helped set up and troubleshoot the simulation input files, GH supported the mesh refinement and time step optimization and performed the RSF analysis in the supplementary material and AZ supervised the study. All authors collaborated on the writing.

Competing interests. The authors declare no competing interests.

References

Bekesi, E., Struijk, M., Bonte, D., Veldkamp, H., Limberger, J., Fokker, P.A., Vrijlandt, M. & Wees, J.D., 2020. An updated geothermal model of the Dutch subsurface based on inversion of temperature data. *Geothermics* **88**: 101880.

Blackwell, D. & Steele, J., 1989. Heat flow and geothermal potential of Kansas. *Kansas Geological Survey Bulletin* **226**: 267–295.

Blake, G.R., 2008. Particle density. *In:* Chesworth W. (ed): *Encyclopedia of soil science. Encyclopedia of earth sciences series.* Springer (Dordrecht). DOI: 10.1007/978-1-4020-3995-9_406.

Blöcher, G., Cacace, M., Jacquey, A.B., Zang, A., Heidbach, O., Hofmann, H., Kluge, C. & Zimmermann, G., 2018. Evaluating micro-seismic events triggered by reservoir operations at the geothermal site of Groß Schönebeck (Germany). *Rock Mechanics and Rock Engineering* **51**(10): 3265–3279. DOI: 10.1007/s00603-018-1521-2.

Blöcher, M.G., Zimmermann, G., Moeck, I., Brandt, W., Hassanzadegan, A. & Magri, F., 2010. 3D numerical modelling of hydrothermal processes during the lifetime of a deep geothermal reservoir. *Geofluids* **10**(3): 406–421. DOI: 10.1111/j.1468-8123.2010.00284.x.

Bonté, D., van Wees, J.-D. & Verweij, J.M., 2012. Subsurface temperature of the onshore Netherlands: new temperature data set and modelling. *Netherlands Journal of Geosciences / Geologie en Mijnbouw* **91**(4): 491–515.

Broothaers, M., Bos, S., Lagrou, D., Harcouët-Menou, V. & Laenen, B.,2019. Lower Carboniferous limestone reservoir in northern Belgium: structural insights from the Balmatt project in Mol. *In: European Geothermal Congress Proceedings*, The Hague.

Buijze, A.J.L., 2020. Numerical and experimental simulation of fault reactivation and earthquake rupture applied to induced seismicity in the Groningen gas field. Doctoral Dissertation. Utrecht University.

Buijze, L., van Bijsterveldt, L., Cremer, H., Paap, B., Veldkamp, H., Wassing, B.T., Wees, J.D., Yperen G.C., N., Jaarsma, B. & Heege, J.H., 2020. Review of induced seismicity in geothermal systems worldwide and implications for geothermal systems in the Netherlands. *Netherlands Journal of Geosciences* **98**: e13.

Buijze, L., van den Bogert, P.A.J., Wassing, B.B.T., Orlic, B. & ten Veen, J., 2017. Fault reactivation mechaisms and dynamic rupture modelling of depletion-induced seismic events in a Rotliegend gas reservoir. *Netherlands Journal of Geosciences – Geologie en Mijnbouw* **96**(5): 131–148. DOI: 10.1017/njg.2017.27.

Cacace, M. & Blöcher, G, 2015. MeshIt-a software for three dimensional volumetric meshing of complex faulted reservoirs. *Environmental Earth Sciences* **74**(6): 5191–5209. DOI: 10.1007/s12665-015-4537-x.

Cacace, M., Hofmann, H. & Shapiro, S.A., 2021. Projecting seismicity induced by complex alterations of underground stresses with applications to geothermal systems. *Scientific Reports* **11**(1): 23560.

Cacace, M. & Jacquey, A.B., 2017. Flexible parallel implicit modelling of coupled thermal hydraulic mechanical processes in fractured rocks. *Solid Earth* **8**(5): 921–941.

Candela, T., Osinga, S., Ampuero, J.-P., Wassing, B., Pluymaekers, M., Fokker, P. A., van Wees, J.-D., de Waal, H.A. & Muntendam-Bos, A.G., 2019. Depletion-Induced seismicity at the Groningen gas field: Coulomb rate-and-state models including differential compaction effect. *Journal of Geophysical Research: Solid Earth*, **124**, 7081–7104. https://doi.org/10.1029/2018JB016670

Daniilidis, A., Doddema, L. & Herber, R., 2016. Risk assessment of the Groningen geothermal potential: From seismic to reservoir uncertainty using a discrete parameter analysis. *Geothermics* **64**: 271–288. DOI: 10.1016/j.geothermics.2016.06.014.

De Jager, J., 2007. Geological development. *In:* Wong, T., Batjes, D.A.J. & de Jager J. (eds): *Geology of the Netherlands.* Royal Netherlands Academy of Arts and Sciences (Amsterdam): 5–26.

De Simone, S., Vilarrasa, V., Carrera, J., Alcolea, A. & Meier, P., 2013. Thermal coupling may control mechanical stability of geothermal reservoirs during cold water injection. *Physics and Chemistry of the Earth* **64**: 117–126. DOI: 10.1016/j.pce.2013.01.001.

Delage, P., 2013. On the thermal impact on the excavation damaged zone around deep radioactive waste disposal. *International Journal of Rock Mechanics and Geotechnical Engineering* **5**(3): 179–190. DOI: 10.1016/j.jrmge.2013.04.002.

Destress, 2021. Available at http://www.destress-h2020.eu/en/demonstration-sites/middenmeer

Dinoloket, 2021. Available at https://www.dinoloket.nl/en/subsurface-models

Doddema, L., 2012. *The influence of reservoir heterogeneities on geothermal doublet performance*. Master Thesis. University of Groningen.

Duin, E.J.T., Doornenbal, J.C., Rijkers, R.H.B., Verbeek, J.W. & Wong, T.E., 2006. Subusrface structure of the Netherlands – results of recent onshore and offshore mapping. *Netherlands Journal of Geosciences – Geologie en Minjbouw* **85**(4): 245–276. DOI: 10.1017/S0016774600023064.

Evans Jr., H.T., 1979. The thermal expansion of Anhydrite to 1000°C. *Physics and Chemistry of Minerals* **4**(1): 77–82. DOI: 10.1007/BF00308361.

Falzone, A.J. & Stacey, F.D., 1982. Measurements of thermal expansions of small mineral crystals. *Physics and Chemistry of Minerals* **8**(5): 212–217.

Fei, Y., 1995. Thermal Expansion. In Mineral Physics & Crystallography, T.J. Ahrens (Ed.). https://doi.org/10.1029/RF002p0029

Foulger, G.R., Wilson, M.P., Gluyas, J.G., Julian, B.R. & Davies, R.J., 2018. Global review of human-induced earthquakes. *Earth-Science Reviews* **178**: 438–514. DOI: 10.1016/j.earscirev.2017.07.008.

Francke, H., Kraume, M. & Saadat, M., 2013. Thermal-hydraulic measurements and modelling of the brine circuit in a geothermal well. *Environmental Earth Sciences* **70**(8): 3481–3495. DOI: 10.1007/s12665-013-2612-8.

Fuchs, S., Balling, N. & Förster, A., 2015. Calculation of thermal conductivity, thermal diffusivity and specific heat capacity of sedimentary rocks using petrophysical well logs. *Geophysical Journal International* **203**(3): 1977–2000. DOI: 10.1093/gji/ggv403.

Ghabezloo, S. & Sulem, J., 2009. Stress dependent thermal pressurization of a fluid-saturated rock. *Rock Mechanics and Rock Engineering* **42**(1): 1–24. DOI: 10.1007/s00603-008-0165-z.

Ghassemi, A., Tarasovs, S. & Cheng, A.H.-D., 2007. A 3-D study of the effects of thermomechanical loads on fracture slip in enhanced geothermal reservoirs. *International Journal of Rock Mechanics and Mining Sciences* **44**(8): 1132–1148. DOI: 10.1016/j.ijrmms.2007.07.016.

Griffith, J., 1936. Thermal expansion of typical American rock. Iowa State College of Agriculture and Mechanics Arts. *Iowa Engineering Experiments* **35**(19): 24.

Guglielmi, Y., Cappa, F., Avouac, J.P., Henry, P. & Elsworth, D., 2015. Seismicity triggered by fluid injection-induced aseismic slip. *Science* **348**(6240): 1224–1226.

Guises, R., Embry, J.-M. & Barton, C., 2015. Dynamic geomechanical modelling to assess and minimize the risk for fault slip during reservoir depletion of the groningen field. Baker Hughes project report for NAM, project reference: NAM0001, Revision No. 1, June 2015.

Hassanzadegan, A., Blöcher, G., Zimmermann, G. & Milsch, H., 2012. Thermoporoelastic properties of Flechtinger sandstone. *International Journal of Rock Mechancis and Mining Sciences* **49**: 94–104. DOI: 10.1016/j.ijrmms.2011.09.002.

Heidbach, O., Rajabi, M., Reiter, K. & Ziegler, M., 2016. World Stress Map 2016. GFZ Data Services. https://doi.org/10.5880/WSM.2016.002

Huenges, E., Ellis, J., Welter, S., Westaway, R., Min, K.B., Genter, A., Brehme, M., Hofmann, H., Meier, P., Wassing, B. & Marti, M., 2020. Demonstration of soft stimulation treatments in geothermal reservoirs. *In: Proceedings of the world geothermal congress* (Vol. **1**).

Hunfeld, L.B., Chen, J., Hol, S., Niemeijer, A.R. & Spiers, C.J., 2020. Healing behaviour of simulated fault gouges from the Groningen gas field and implications for induced fault reactivation. *Journal of Geophysical Research Solid Earth* **125**(7): e2019JB018790. DOI: 10.1029/2019JB018790.

Hunfeld, L.B., Niemeijer, A.R. & Spiers, C.J., 2017. Frictional properties of simulated fault gouges from the seismogenic Groningen gas field under in situ P-T-Chemical conditions. *Journal of Geophysical Research Solid Earth* **122**(11): 8969–8989. DOI: 10.1002/2017JB014876.

Hurter, S. & Schellschmidt, R., 2003. Atlas of geothermal resources in Europe. *Geothermics* **32**(4-6): 779–787. DOI: 10.1016/S0375-6505(03)00070-1.

Hutka, G.A., Cacace, M., Hofmann, H., Zang, A., Wang, L. & Ji, Y., 2023. Numerical investigation of the effect of fluid pressurization rate on laboratory-scale injection-induced fault slip. *Scientific Reports* **13**(1): 4437.

Jacquey, A.B. & Cacace, M., 2017. GOLEM, a MOOSE-based application. DOI: 10.5281/zenodo.999401.

Jaeger, J.C., Cook, N.G.W. & Zimmerman, R.W., 2007. *Fundamentals of rock mechanics*. Fourth Edition. Blackwell Publishing (Oxford): 475 pp.

Jansen, J.D. & Meulenbroek, B., 2022. Induced aseismic slip and the onset of seismicity in displaced faults. *Netherlands Journal of Geosciences* **101**: e13.

Kansy, A., 2007. Einfluss des Biot-Parameters auf das hydraulische Verhalten von Steinsalz unter der Berücksichtigung des Porendrucks. Dissertation. TU Clausthal, Fakultät für Energie- und Wirtschaftswissenschaften (Clausthal).

Kivi, I.R., Pujades, E., Rutqvist, J. & Vilarrasa, V., 2022. Cooling-induced reactivation of distant faults during long-term geothermal energy production in hot sedimentary aquifers. *Scientific Reports* **12**: 2065. DOI: 10.1038/s41598-022-06067-0.

Lele, S.P., Garzon, J.L., Hsu, S.-Y., DeDontney, N.L., Searles, K.H. & Sanz, P.F., 2015. Groningen 2015 Geomechanical analysis. NAM report, November 2015.

Lemmon, E.W., Bell, I.H., Huber, M.L. & McLinden, M.O., 2018. *NIST Standard Reference Database 23: Reference Fluid Thermodynamic and Transport Properties-REFPROP, Version 10.0*. National Institute of Standards and Technology, Standard Reference Data Program (Gaithersburg).

McTigue, D.F., 1986. Thermoelastic response of fluid-saturated porous rock. *Journal of Geophysical Research: Solid Earth* **91**(B9): 9533–9542. DOI: 10.1029/JB091iB09p09533.

Mechelse, E., 2017. The in-situ stress field in the Netherlands: regional trends, local deviations and an analysis of the stress regimes in the northeast of the Netherlands. Master Thesis. TU Delft.

Mijnlieff, H.F., 2020. Introduction to the geothermal play type and reservoir geology of the Netherlands. *Netherlands Journal of Geosciences* **99**(e2). DOI: 10.1017/njg.2020.2.

Missal, C., 2019. Numerisches Modell zur Entwicklung der Permeabilität von Steinsalz in Abhängigkeit von Schädigung, Fluiddruck und Spannungszustand. PhD Thesis, Technische Universität Braunschweig, 171 pages, DOI: 10.24355/dbbs.084-201903041301-0.

Mohammed, A.K.A., 2020. A review: controls on sandstone permeability during burial and its measurements comparison—example, Permian Rotliegend Sandstone. *Modeling Earth Systems and Environment* **6**(2): 591–603. DOI: 10.1007/s40808-019-00704-w.

Monfared, M., Sulem, J. & Delage, P., 2011. A laboratory investigation on thermal properties of the opalinus claystone. *Rock Mechanics and Rock Engineering* **44**: 735. DOI: 10.1007/s00603-011-0171-4.

Moore, J., McLennan, J., Allis, R., Pankow, K., Simmons, S., Podgorney, R. & Rickard, W., 2019. The Utah Frontier Observatory for Research in Geothermal Energy (FORGE): an international laboratory for enhanced geothermal system technology development. *In: 44th Workshop on Geothermal Reservoir Engineering*. Stanford University (Stanford, CA): 11–13.

Morris, A., Ferrill, D.A. & Henderson, D.B., 1996. Slip-tendency analysis and fault reactivation. *Geology* **24**: 275–278.

Norbeck, J., Latimer, T., Gradl, C., Agarwal, S., Dadi, S., Eddy, E., Fercho, S., Lang, C., McConville, E., Titov, A., Voller, K. & Woitt, M., 2023. A review of drilling, completion, and stimulation of a horizontal geothermal well system in North-Central Nevada. *In: Proceedings of the 48th Workshop on Geothermal Reservoir Engineering*, Stanford University, Stanford, CA, February 6–8 2023, SGP-TR-224.

Osinga, S. & Buik, N., 2019. Stress field characterization in the Dinantian carbonates in the Dutch subsurface. TNO & IF Technology. Report by SCAN. Available at https://scanaardwarmte.nl/results/stress-field-characterization-in-the-dinantian-carbonates-in-the-dutch-subsurface/

Palciauskas, V.V. & Domenico, P.A, 1982. Characterization of drained and undrained response of thermally loaded repository rocks. *Water Resources Research* **18**(2): 281–290. DOI: 10.1029/WR018i002p00281.

Pijnenburg, R.P.J., Verberne, B.A., Hangx, S.J.T. & Spiers, C.J., 2019. Inelastic deformation of the Slochteren sandstone: stress-strain relations and implications for induced seismicity in the Groningen gas field. *Journal of Geophysical Research Solid Earth* **124**(5): 5254–5282. DOI: 10.1029/2019JB017366.

Plevová, E., Vaculiková, L., Kozusníková, A., Danek, T., Pleva, M., Ritz, M. & Martynková, G.S., 2011. Thermal study of sandstones from different Czech localities. *Journal of Thermal Analysis and Calorimetry* **103**(3): 835–843. DOI: 10.1007/s10973-010-1129-6.

Ramsay, J.G. & Lisle, R.J, 2000. Applications of continuum mechanics in structural geology. *In: Techniques of modern structural geology* (Vol. **3**). Academic Press (London).

Richter, A., 2019. The Top10 Geothermal Countries 2019: based on installed generation capacity (MWe). *Think GeoEnergy-Geothermal Energy News*, Jan. 27, 2020. Available at https://www.thinkgeoenergy.com/the-top-10-geothermal-countries-2019-based-on-installed-generation-capacity-mwe/

Schmitt, D.R., 2015. 11.03 - Geophysical properties of the near surface earth: seismic properties. *In:* Schubert G. (ed): *Treatise on geophysics.* Second Edition. Elsevier (Amsterdam): 43–87. ISBN 9780444538031. DOI: 10.1016/B978-0-444-53802-4.00190-1.

Skinner, B.J., 1966. Thermal expansion. *Geological Society of America Memoir* **97**: 75–96.

Slizowski, J., Nagy, S., Burliga, S., Serbin, K. & Polanski, K., 2015. Laboratory investigations of geotechnical properties of rock salt in Polish salt deposits. *In:* Roberts, L., Mellegard, K. & Hansen, F. (eds): *Mechanical behavior of salt VIII: Proceedings of the Conference on Mechanical Behavior of Salt, SALTMECH VIII: Rapid City, USA, 26–28 May 2015.* CRC Press Taylor & Francis Group (Boca Raton): 33–38. ISBN: 978-1-138-02840-1; e-ISBN: 978-1-315-67885-6.

Somerton, W.H., 1992. *Thermal properties and temperature related behaviour of rock/fluid systems.* Elsevier (New York).

Srinivasan, R., 1955. The thermal expansion of calcite from room temperature up to 400°C. *Proceedings of the Indian Academy of Sciences - Section A* **42**(2): 81–85. DOI: 10.1007/BF03053495.

TNO-GSN, 2021. *Zechstein Group. Stratigraphic Nomenclature of the Netherlands, TNO – Geological Survey of the Netherlands.* Available at http://www.dinoloket.nl/en/stratigraphic-nomenclature/zechstein-group, last accessed on 28 February 2021.

TNO, 2015. Integrated pressure information system for the onshore and offshore Netherlands. *Final report*, 83 pp.

Urquhart, A. & Bauer, S., 2015. Experimental determination of single-crystal halite thermal conductivity, diffusivity and specific heat from −75 °C to 300 °C. *International Journal of Rock Mechanics and Mining Sciences* **78**: 350–352. DOI: 10.1016/j.ijrmms.2015.04.007.

Van Eijs, R.M.H.E. 'Neotectonic stresses in the permian slochteren formation of the groningen field 2015. NAM report EP201510210531.

Van Leverink, D. & Geel, K., 2019. Fracture characterization of the Dinantian carbonates in the Dutch subsurface. Report by SCAN, November 2019.

Van Wees, J.-D., Fokker, P.A., Van Thienen-Visser, K., Wassing, B.B.T., Osinga, S., Orlic, B., Ghouri, S.A., Buijze, L. & Pluymaekers, M., 2017. Geomechanical models for induced seismicity in the Netherlands: inferences from simplified analytical, finite element and rupture model approaches. *Netherlands Journal of Geosciences* **96**(5): s183–s202.

Veldkamp, J.G., Goldberg, T.V., Bressers, P.M.M.C. & Wilschut, F., 2016. Corrosion in Dutch geothermal systems. TNO report R10160, 15 March 2016: 105.

Verweij, J., Simmelink, H., Underschultz, J. & Witmans, N., 2012. Pressure and fluid dynamic characterisation of the Dutch subsurface. *Netherlands Journal of Geosciences - Geologie En Mijnbouw* **91**(4): 465–490. DOI: 10.1017/S0016774600000342.

Vörös, R. & Baisch, S., 2022. Induced seismicity and seismic risk management – a showcase from the Californië geothermal field (the Netherlands). *Netherlands Journal of Geosciences* **101**(e15). DOI: 10.1017/njg.2022.12.

Wang, Y., Khait, M., Voskov, D., Saeid, S. & Bruhn, D., 2019. Benchmark test and sensitivity analysis for Geothermal Applications in the Netherlands. *In: Proceedings of the 44th Workshop on Geothermal Reservoir Engineering, Stanford University,* Stanford, CA, Febaruary 11–13 2019, SGP-TR-214.

Waples, D.W. & Waples, J.S., 2004. A review and evaluation of specific heat capacities of rocks, minerals, and subsurface fluids. Part 1: minerals and nonporous rocks. *Natural Resources Research* **13**(2): 97–122. DOI: 10.1023/B:NARR.0000032647.41046.e7.

Wassing, B.B.T., Buijze, L., Ter Heege, J.H., Orlic, B. & Osinga, S., 2017, June. The impact of viscoelastic caprock on fault reactivation and fault rupture in producing gas fields. In: *ARMA US Rock Mechanics/Geomechanics Symposium (ARMA-2017).* ARMA.

Wassing, B.B.T., Candela, T., Osinga, S., Peters, E., Buijze, L., Fokker, P.A. & Van Wees, J.D., 2021. Time-dependent seismic footprint of thermal loading for geothermal activities in fractured carbonate reservoirs. *Frontiers in Earth Science* **9**: 685841.

Willems, C., Vondrak, A., Mijnlieff, H., Donselaar, M. & Van Kempen, B., 2020. Geology of the Upper Jurassic to Lower Cretaceous geothermal aquifers in the West Netherlands Basin – an overview. *Netherlands Journal of Geosciences* **99**: E1. DOI: 10.1017/njg.2020.1.

Willems, C.J.L., Nick, H.M., Weltje, G.J. & Bruhn, D.F., 2017. An evaluation of interferences in heat production from low enthalpy geothermal doublet systems. *Energy* **135**: 500–512. DOI: 10.1016/j.energy.2017.06.129.

Zang, A., Wagner, C.F. & Dresen, G., 1996. Acoustic emission, microstructure, and damage model of dry and wet sandstone stressed to failure. *Journal of Geophysical Research Solid Earth* **101**(B8): 17507–17521. DOI: 10.1029/96JB01189.

Zhang, C.-L., Rothfuchs, T., Jockwer, N. & Komischke, M., 2007. Thermal effects on the opalius clay. Final Report. GRS – 224. ISBN 978-3-931995-98-0. Available at https://www.grs.de/sites/default/files/pdf/grs-224_0.pdf

Zhang, D., Jeannin, L., Hevin, G., Egermann, P., Potier, L. & Skoczylas, F., 2018. Is salt a poro-mechanical material? *In: 52nd US Rock Mechanics / Geomechanics Symposium, Seattle, Washington, USA, 17–20 June 2018.* ARMA 18-0423.

Zimmerman, R.W., 2000. Coupling in poroelasticity and thermoelasticity. *International Journal of Rock Mechanics and Mining Sciences* **37**(1-2): 79–87. DOI: 10.1016/j.ijrmms.2011.11.002.

Zoback, M.D., 2007. *Reservoir geomechanics: earth stress and rock mechanics applied to exploration, production and wellbore stability.* Cambridge University Press (Cambridge).